

A First-Principles Investigation of Thermoelectric Performance of 2D and 3D Materials

Thesis submitted

**In partial fulfilment of the requirements for the
Degree of**

**MASTER OF SCIENCE
in
APPLIED PHYSICS**

**Submitted By:
Stephen S. Mathew
(2K22/MSCPHY/61)**

**Under the supervision of
Dr. Mukhtiyar Singh
(Delhi Technological University)**



Department of Applied Physics

DELHI TECHNOLOGICAL UNIVERSITY

(Formerly Delhi College of Engineering)

Shahbad Daultapur, Main Bawana Road, Delhi-110042,

India

May, 2024



DELHI TECHNOLOGICAL UNIVERSITY
(Formerly Delhi College of Engineering)
Shahbad Daultapur, Main Bawana Road, Delhi-42

CANDIDATE'S DECLARATION

I, **Stephen Shaiju Mathew (2K22/MSCPHY/61)** student of MSc Physics, now certify that the work which is being presented in the thesis entitled “**A First-principles Investigation of Thermoelectric Performance of 2D and 3D Materials**” in partial fulfilment of the requirement for the award of the degree of Master in Science, submitted in the Department of Applied Physics, Delhi Technological University is an authentic record of my work carried out during the period from May 2023 to May 2024 under the supervision of Dr. Mukhtiyar Singh. I have not submitted the matter represented in the thesis for the award of any other degree of this or any other institute. The work has been communicated in peer-reviewed Scopus-indexed conferences with the following details:

Title of the Paper (I): Effect of strain on the electronic and thermoelectric properties of Zintl compound KCd_4P_3 : A Density functional theory study

Author names (in the sequence as per research paper): Stephen Shaiju Mathew, Sangeeta, Mukhtiyar Singh

Name of Conference: Recent Advances in Functional Materials (RAFM-2024)

Name of the Journal: Springer Nature Proceedings of RAFM 2024 (Scopus Indexed)

Conference Dates with venue: 2024, March 14-16, Online

Have you registered for the conferences: Yes

Status of paper: Accepted

Date of paper communication: April, 2024

Place: Delhi

Date: 07/06/2024

Stephen Shaiju Mathew
(2k22/MSCPHY/61)



DELHI TECHNOLOGICAL UNIVERSITY
(Formerly Delhi College of Engineering)
Shahbad Daultpur, Main Bawana Road, Delhi42

SUPERVISOR CERTIFICATE

Certified that Stephen Shaiju Mathew (2k22/MSCPHY/61) has carried out the search work presented in this thesis entitled “A First-principles Investigation of Thermoelectric Performance of 2D and 3D Materials” For the award of Masters of Science from the Department of Applied Physics, Delhi Technological University, Delhi under my supervision. The thesis embodies the result of original work, and studies are carried out by the student himself. The content of the thesis does not form the basis for the award of any other degree to the candidate or anybody else from this or any other university.

Place: Delhi

Date:07/06/2024

Signature

Dr. Mukhtiyar Singh
(Supervisor)



DELHI TECHNOLOGICAL UNIVERSITY
(Formerly Delhi College of Engineering)
Shahbad Daulatpur, Main Bawana Road, Delhi-42

ACKNOWLEDGEMENT

I want to express my gratitude and indebtedness to **Dr. Mukhtiyar Singh**, Assistant Professor, Department of Applied Physics, Delhi Technological University for their inspiring guidance, constructive criticism, and valuable suggestions throughout the project.

I would also like to thank **Ms. Sangeeta**, Research Fellow, Department of Applied Physics, Delhi Technological University for her mentorship and for sharing her experience and expertise on this subject. I am thankful for her constant guidance and support. I would also like to thank my laboratory members and friends **Ms. Nidhi Kadhyan, Mr. Ramesh Kumar, Mr Rajesh Kumar** and **Mr. Kulwinder Singh** for their continuous support and understanding. I am also thankful to my family and colleagues for their invaluable support, care, and patience during this project.

Lastly, I would also like to thank the Department of Applied Physics, Delhi Technological University for allowing me to work on this topic.

LIST OF CONFERENCES

Name of Conference: Recent Advances in Functional Materials (RAFM-2024)

Conference Dates: 2024, March 14-16

Mode of the conference: online

Title of the presentation: Effect of strain on the electronic and thermoelectric properties of Zintl compound KCd_4P_3 : A Density Functional Theory Study.

Venue: ATMA RAM SANATAN DHARMA COLLEGE, NEW DELHI

Name of Conference: International Conference on Materials Genome-III

Conference Dates: 2024, February 22-24

Mode of the conference: offline

Title of the poster: The Impact of Strain on Thermoelectric Properties HfNBr Monolayer: A First-Principles Study

Venue: SRM UNIVERSITY, ANDHRA PRADESH

PARTICIPATION RECORD

 **ATMA RAM SANATAN DHARMA COLLEGE** 
UNIVERSITY OF DELHI
Accredited Grade 'A++' By NAAC || All India 6th Rank in NIRF (Ministry of Education)
2nd International Conference on
Recent Advances in Functional Materials (RAFM-2024)
Under the aegis of IQAC and DBT (GoI) star college scheme

Certificate of Oral Presentation




This is to certify that Prof./Dr./Mr./Ms.
STEPHEN SHAIJU MATHEW
Delhi Technological University, New Delhi
has presented his/her research work as oral presentation titled
Effect of strain on the electronic and thermoelectric properties of Zintl compound KCd4P3 using Density functional theory
in 2nd International Conference on "Recent Advances in Functional Materials" (RAFM-2024) organised by Department of Physics under the aegis of IQAC ARSD College, University of Delhi & DBT (GoI) Star College during March 14-16, 2024 via online mode.


Dr. Manish Kumar
Convener, RAFM-2024



Prof. Vinita Tuli
Coordinator, IQAC

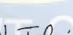

Prof. Gyantosh Kumar Jha
Principal, ARSD College


Certificate No: ARSD/RAFM-2024/OT/168

 **ATMA RAM SANATAN DHARMA COLLEGE** 
UNIVERSITY OF DELHI
Accredited Grade 'A++' By NAAC || All India 6th Rank in NIRF (Ministry of Education)
2nd International Conference on
Recent Advances in Functional Materials (RAFM-2024)
Under the aegis of IQAC and DBT (GoI) star college scheme

Certificate of Best Oral Presentation

This is to certify that Prof./Dr./Mr./Ms.
STEPHEN SHAIJU MATHEW
Delhi Technological University, New Delhi
has presented his/her research work as oral presentation and received **BEST ORAL** Presentation titled
Effect of strain on the electronic and thermoelectric properties of Zintl compound KCd4P3 using Density functional theory
in 2nd International Conference on "Recent Advances in Functional Materials" (RAFM-2024) organised by Department of Physics under the aegis of IQAC ARSD College, University of Delhi & DBT (GoI) Star College during March 14-16, 2024 via online mode.


Dr. Manish Kumar
Convener, RAFM-2024


Prof. Vinita Tuli
Coordinator, IQAC


Prof. Gyantosh Kumar Jha
Principal, ARSD College

Certificate No: ARSD/RAFM-2024/BOP/016



International Conference on Materials Genome -III

ICMG - III

Certificate of Participation

This is to certify that

Stephen .S Mathew

has attended and presented a poster titled

**The Impact of Strain on the Thermoelectric Properties of HfNBr Monolayer:
A First- Principles Study**

in the *International Conference on Materials Genome-III* held at SRM University AP,
Andhra Pradesh, India from 22nd to 24th February, 2024 .

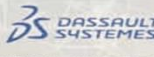
Yoshiyuki Kawazoe

Chairperson
Prof. Yoshiyuki Kawazoe
Tohoku University, Japan

Ranjit Thapa

Convener
Prof. Ranjit Thapa
SRM University-AP, India

Sponsored by



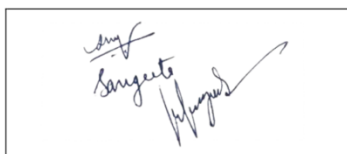
COPYRIGHT FORM

Licence to Publish Proceedings Papers

SPRINGER NATURE

Licensee	Springer Nature Singapore Pte Ltd.	(the 'Licensee')
Title of the Proceedings Volume/Edited Book or Conference Name:	Recent Advances in Functional Materials, Volume 1 - Select Proceedings of RAFM 2024	(the 'Volume')
Volume Editor(s) Name(s):	Dr. Manish Kumar, Dr. Anjani Kumar Singh, Dr. Subhash Sharma, Prof. Devendra Kumar	
Proposed Title of the Contribution:	Effect of strain on the electronic and thermoelectric properties of zintl compound KCD4P3:A Density functional theory study	(the 'Contribution')
Series: The Contribution may be published in the following series	A Springer book series Springer Proceedings in Materials series	
Author(s) Full Name(s):	Stephen Shaiju Mathew, Sangeeta	(the 'Author')
<i>When Author is more than one person the expression "Author" as used in this Agreement will apply collectively unless otherwise indicated.</i>		
Corresponding Author Name:	Mukhtiyar Singh	
Instructions for Authors	https://www.springer.com/gp/authors- editors/conference-proceedings/conference-proceedings- guidelines	(the 'Instructions for Authors')

Signed for and on behalf of the Author



Print Name:

Stephen Shaiju Mathew
Sangeeta
Mukhtiyar Singh

Date:

19/04/2024

Address:

Department of applied Physics, Delhi Technological University, Delhi-110042, India

Email:

mukhtiyarsingh@dtu.ac.in

Springer Nature Singapore Pte Ltd., 152 Beach Road, #21-01/04 Gateway East, Singapore 189721, Singapore
ER_Book_ProceedingsPaper_LTP_ST_v.1.0 (10_2021)

COMMUNICATION RECORD



Sangeeta <sangeetadhull_2k20phdap02@dtu.ac.in>

Recent Advances in Functional Materials- Select Springer Nature Proceedings of RAFM 2024 (Scopus Indexed)

RAFM-2024, Department of Physics ARSD College <rafm@arsd.du.ac.in>
To: "RAFM-2024, Department of Physics ARSD College" <rafm@arsd.du.ac.in>
Bcc: sangeetadhull_2k20phdap02@dtu.ac.in

Mon, May 13, 2024 at 11:24 PM

Dear Author,

Thank you for submitting your manuscript to "Select Springer Nature Proceedings of RAFM 2024 (Scopus Indexed)". All submissions have to undergo a stringent pre-screening process. Only the papers that have novelty in terms of plagiarism less than 10% and high potential to attract a broad audience and to inspire new studies will be selected for peer review. We are in the process of initial screening and peer review. This email is for your reference and acknowledgement of receiving your manuscript to "Select Springer Nature Proceedings of RAFM 2024 (Scopus Indexed)".

Kind regards,

Editorial Team,
Select Springer Nature Proceedings of RAFM 2024

ACCEPTANCE LETTER



Dr. Mukhtiyar Singh <mukhtiyarsingh@dtu.ac.in>

Decision Letter (RAFM_14)

1 message

RAFM-2024, Department of Physics ARSD College <rafm@arsd.du.ac.in>
To: mukhtiyarsingh@dtu.ac.in
Cc: Subhash Sharma <subhash1jiit@gmail.com>, subhash@cryn.unam.mx

Wed, Jun 5, 2024 at 9:05 PM

Ms. Ref. No.: RAFM_14

Title: Effect of strain on the electronic and thermoelectric properties of Zintl compound KCd_4P_3 : A Density functional theory study

Dear Mr. Mukhtiyar Singh

I am pleased to inform you that your paper " Effect of strain on the electronic and thermoelectric properties of Zintl compound KCd_4P_3 : A Density functional theory study " **Select Springer Nature Proceedings of RAFM 2024 (Scopus Indexed)**".

Regards

Editor, RAFM-2024

ABSTRACT

In this work through first-principle calculations, we investigate and enhance the thermoelectric performance of monolayer and bulk materials from three different families of compounds. We propose two strategies to enhance thermoelectric performance: carrier optimisation and strain engineering.

Enhancement through carrier optimisation

we investigate the electronic, structural, elastic, and TE properties of the AgSbS₂ monolayer, using density functional theory in conjunction with Boltzmann transport theory. In this study, we proposed our strategy to increase the figure of merit (ZT) by optimizing the carrier concentrations. The monolayer of AgSbS₂ is found to be both mechanically and thermodynamically stable. The calculated electronic band structure shows a semiconducting-like behaviour of AgSbS₂ with an indirect band gap of 1.31 eV using the Heyd-Scuderia-Ernzerhof (HSE06) exchange-correlation functional. The investigated monolayer is found to be anisotropic, hence we analysed its thermoelectric properties at various carrier concentrations along a - and b -directions. It attained a high value of Seebeck coefficient of 360 μVK^{-1} in the a -direction and 370 μVK^{-1} in the b -direction at room temperature. The maximum ZT of AgSbS₂ monolayer at an optimized carrier concentration of $5 \times 10^{18} \text{ cm}^{-3}$ is found to be as high as 0.3 and 0.5 at 300 K in both a - and b -directions, respectively, for the n-type monolayer,. The high ZT values of AgSbS₂ indicate its potential for room-temperature energy harvesting applications.

Enhancement through Strain engineering

Through first-principles calculations in conjunction with the semiclassical Boltzmann transport theory we study the thermoelectric performance of KCd₄P₃. The ternary KCd₄P₃ phase crystallizes in the centrosymmetric rhombohedral space group $R\bar{3}m$. A good match is shown between the calculated results, such as lattice constants and bond

lengths, with the results calculated experimentally . As the generalized gradient approximation generally underestimates the band gap, therefore, we have utilized a more accurate functional i.e., Tran Blaha modified Becke Johnson approach and obtained a direct band gap of 0.66 eV of unstrained KCd_4P_3 . The positive value of the Seebeck coefficient which goes as high as 248 $\mu\text{V}/\text{K}$ at room temperature identifies KCd_4P_3 as a p-type semiconducting material. We propose method to increase power factor and TE performance via strain which is useful for tuning TE parameters independently, leading to a high figure of merit of 0.78 at 300 K.

TABLE OF CONTENTS

<i>CANDIDATE'S DECLARATION</i>	<i>ii</i>
<i>SUPERVISOR CERTIFICATE</i>	<i>iii</i>
<i>ACKNOWLEDGEMENT</i>	<i>iv</i>
<i>LIST OF CONFERENCES</i>	<i>v</i>
<i>PARTICIPATION RECORD</i>	<i>vi</i>
<i>COPYRIGHT FORM</i>	<i>viii</i>
<i>COMMUNICATION RECORD</i>	<i>ix</i>
<i>ACCEPTANCE LETTER</i>	<i>x</i>
<i>ABSTRACT</i>	<i>xi</i>
<i>TABLE OF CONTENTS</i>	<i>xiii</i>
<i>LIST OF TABLES</i>	<i>xv</i>
<i>LIST OF FIGURES</i>	<i>xvi</i>
<i>LIST OF SYMBOLS AND ABBREVIATIONS</i>	<i>xviii</i>
<i>CHAPTER 1</i>	<i>1</i>
<i>INTRODUCTION</i>	<i>1</i>
1.1 Thermoelectric materials and energy harvesting	<i>1</i>
1.1.1 Thermoelectric figure of merit (ZT)	<i>2</i>
1.2 Two-dimensional Materials	<i>4</i>
1.3 Bulk materials.....	<i>6</i>
<i>CHAPTER 2</i>	<i>9</i>
<i>METHODOLOGY</i>	<i>9</i>
2.1. Computational Methods.....	<i>9</i>
2.1.1. Density Functional Theory (DFT)	<i>9</i>
2.1.2. Exchange correlation functional	<i>12</i>
2.1.3. Generalised gradient approximation	<i>14</i>
2.1.4. The LAPW method -	<i>14</i>
2.1.5. Boltzmann Transport Theory	<i>14</i>
2.2. Computer programs	<i>16</i>
2.2.1 VASP	<i>16</i>
2.2.2 WIEN2k	<i>17</i>
2.2.3 BoltZTraP2	<i>18</i>

2.2.4 AMSET	18
CHAPTER 3	21
LITERATURE SURVEY	21
3.1 Survey for AgSbS ₂ monolayer	21
3.1.1 . selection of a suitable silver-based dichalcogenide	24
3.2 Survey of KCd ₄ P ₃	25
Half-Heusler	25
3.2.1 Selection of a suitable Zintl compound	27
3.3 Motivation	28
CHAPTER 4	29
RESULTS AND DISCUSSION	29
4.1 Results and discussion for AgSbS ₂ monolayer	29
4.1.1 Structural properties	29
4.1.2 Computational details	30
4.1.3 Stability Analysis	31
4.1.4 Electronic Structure	33
4.1.5 ZT enhancement through doping.....	35
4.1.6 Transport properties.....	36
4.1.7 Thermoelectric Figure of Merit	40
4.2 Results and Discussion for KCD ₄ P ₃	41
4.2.1 Structural properties	41
4.4.2 Computational details	42
4.2.3 Electronic structure	42
4.2.4 ZT enhancement through strain engineering	45
4.2.5 Transport properties.....	45
4.2.6 Thermoelectric figure of merit	48
CONCLUSION AND FUTURE SCOPE	50
REFERENCES.....	52
PROOF AND SCOPUS INDEXING	61
PLAGIARISM.....	62

LIST OF TABLES

S. No.	Table No.	Title of the Table	Page No.
1	Table 1	Obtained structural parameters (a and b in \AA and V in \AA^3) and bond lengths (in \AA) of AgSbS_2 in comparison with its iso-structure CuSbS_2	30
2	Table 2	Obtained Young's Modulus (Y), Bulk Modulus (B), Shear Modulus (G) in Nm^{-1} , the transverse (v_t) and longitudinal (v_l) sound velocity, mean sound velocity (v_m) in Kms^{-1} and Debye temperature (θ_D) in K of AgSbS_2 .	33
3	Table 3	Obtained lattice constants (a and c in \AA), volume (V in \AA^3) and bond lengths (in \AA) of KCd_4P_3 in comparison with its experimental results.	42

LIST OF FIGURES

S. No.	Fig. No.	Title of the Figure	Page No.
1	1	Different sources of waste heat energy	2
2	2	different Two-dimensional Materials	5
3	3	The theme of Density functional theory	9
4	4	Scattering of particles in a crystal structure	15
5	5	The Logo of VASP	17
6	6	The Logo of WIEN2k software	17
7	7	The Logo of AMSET	20
8	8	(a)Top view of the monolayer structure of AgSbS ₂ (b) The side view of the monolayer structure of AgSbS ₂	30
9	9	Electronic band structure of AgSbS ₂ (a) using PBE (b) using HSE06	34
10	10	(a)The total Density of States(b)The partial Density of States of AgSbS ₂ using HSE06 functional	35
11	11	Scattering rates due to different scatterings in variation with carrier concentration of AgSbS ₂ for (a) p-type at 300 K (b) n-type at 300 K	36
12	12	The Carrier Mobility due to different scatterings in variation with carrier concentration for (a) p-type at 300 K and (b) n-type at 300 K	37
13	13	(a) The Seeback coefficient (b) the electrical conductivity (c) the electronic contribution for thermal conductivity (d) the power factor for both p- and n-type AgSbS ₂ along <i>a</i> -and <i>b</i> -direction at 300 K	39

14	14	The TE Figure of Merit at 300 K in the <i>a</i> - and <i>b</i> direction in variation with carrier concentration for n- and p-type	40
15	15	The side view of the KCD ₄ P ₃ bulk structure	41
16	16	Electronic band structure (b)DOS of KCD ₄ P ₃ (c) PDOS of KCD ₄ P ₃	44
17	17	Electronic band structure of KCD ₄ P ₃ with (a) 2% strain (b) 4% strain (c) -2% strain (d) -4% strain	44
18	18	S/τ of KCD ₄ P ₃ (a) in the <i>a</i> -direction (b) in the <i>c</i> -direction	46
19	19	σ/τ of KCD ₄ P ₃ (a) in the <i>a</i> -direction (b) in the <i>c</i> -direction	46
20	20	$\kappa e/\tau$ of KCD ₄ P ₃ (a) in the <i>a</i> -direction (b) in the <i>c</i> -direction	47
21	21	$S^2\sigma$ of KCD ₄ P ₃ (a) in the <i>a</i> -direction (b) in the <i>c</i> -direction	48
22	22	ZT of KCD ₄ P ₃ (a) in the <i>a</i> -direction (b) in the <i>c</i> -direction	49

LIST OF SYMBOLS AND ABBREVIATIONS

S. No.	Acronym/Symbol	Full Form
1	TMDs	Transition Metal Dichalcogenides
2	TE	Thermoelectric
3	ZT	Thermoelectric figure of merit
4	DFT	Density Functional Theory
5	HSE06	Heyd-Scuderia-Ernzerhof
6	LDA	Local Density Approximations
7	GGA	Generalised Gradient Approximations
8	PBE	Perdew-Burke-Ernzerhof
9	BTE	Boltzmann transport equations
10	DOS	Density of States
11	PDOS	Projected Density of States
12	CRTA	Constant relaxation time approach
13	E_g	Band-Gap
14	Å	Angstrom
15	eV	electron-volt
16	HH	Half Heuslers
17	RBA	Rigid band approximation
18	Γ	Gamma
19	Cu	Copper
20	Pb	Lead
21	TB-mBJ	Tran Blaha modified Becke Johnson
22	LAPW	Linear augmented plane wave

23	$C_{11}, C_{22}, C_{12}, C_{21}, C_{66}$	Elastic constants
24	CBM	Conduction band minimum
25	VBM	Valence band maximum
26	τ	Constant relaxation time
27	KSE	Kohn-Sham equations
28	VB	Valence band
39	CB	Conduction Band
30	AgSbS_2	Silver antimony disulphide
31	KCd_4P_3	Potassium quadra-Cadmium tri-phosphide
32	PAW	Projected Augmented wave
33	μ	mobility
34	L	Lorenz number
35	RBZn_4P_3	Rubidium-quadra-zinc-triphosphide
36	$n(\mathbf{r})$	Electron density
37	E_{coh}	Cohesive energy

CHAPTER 1

INTRODUCTION

1.1 Thermoelectric materials and energy harvesting

In a world grappling with excessive fossil fuel consumption and its detrimental environmental impacts, achieving a net zero target requires balancing greenhouse gas emissions with removal efforts. To achieve this, developing clean and secure energy alternatives is imperative. New technologies can play a pivotal role in energy generation and storage. These encompass diverse areas such as photovoltaics, wind and water turbines, and energy-efficient technologies like low-loss electronics, piezoelectrics and thermoelectrics (TEs) [1]. Thermoelectricity refers to phenomena that involve the direct and thermodynamically reversible exchange of thermal energy to electricity or vice versa. The Seebeck, Peltier, and Thomson effects are three distinct phenomena that make up thermoelectricity and are named after the researchers who first identified them in the late 19th century. TE materials, for instance, can efficiently convert waste heat into usable electrical energy, powering TE generators[2]. TE devices show unique advantages compared to other energy conversion devices, including stability, long service life, and noiselessness. TE materials harness temperature differentials to produce electrical energy, offering a means of achieving fully electric heating and cooling technology devoid of mechanical components or refrigerants. An additional benefit of this technology lies in its capability to capture residual heat from various phenomena and convert them into electricity. Considering that approximately 2/3 of primary energy is dissipated as heat, using thermoelectric materials can efficiently capture and convert a significant portion of this wasted heat into valuable electrical power [3].

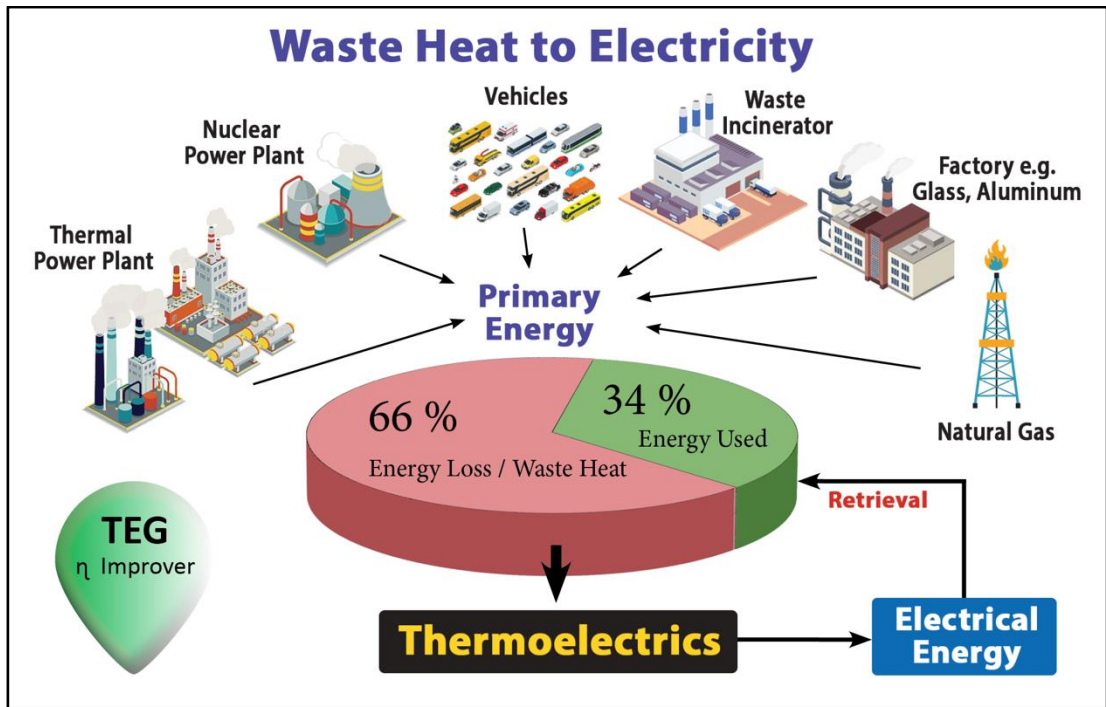


Figure 1: Different sources of waste heat energy(Taken from K.Zeb., *et al.*, 2017. A Survey of Waste and Heat Recovery. Renewable and Sustainable Energy Reviews, Vol75,1142-1145.)

1.1.1 Thermoelectric figure of merit (ZT)

ZT represents the efficiency of TE material and can be calculated from the formula $ZT = S^2\sigma T/\kappa$, S denotes the Seebeck coefficient, σ represents electrical conductivity, where T is the absolute temperature, and κ encompasses the combined effects of electronic (κ_e) and lattice (κ_l) contributions to thermal conductivity. Achieving an optimal ZT necessitates a high power factor ($S^2\sigma$) and reduced κ value. A significant challenge lies in optimizing $S^2\sigma$ and κ_e , as they are interdependent with each other through the carrier concentration[4]. Various strategies have been devised to overcome this challenge to decouple these parameters. These include increasing the power factor via carrier concentration adjustments, tuning band structures, and reducing lattice thermal conductivity through dimensional reduction or introducing defects [5].

The Seebeck effect is the phenomenon of the development of electromotive force (emf) across two sites of material as their temperatures differ, the emf is known as the thermoelectric emf. The Seebeck coefficient is the ratio of this emf and the corresponding temperature change in temperature [6]. A thermocouple gauges the difference between the potential at the hot and cold ends of two different materials. The potential difference between the cold and hot ends is proportional to the difference in temperature across these ends. The first experiments revealing this effect were performed by Alessandro Volta in 1794. The Seebeck effect, like any other emf, produces measurable currents or voltages. $J = \sigma (-\nabla V + E_{emf})$ is the current density(local), where σ conductivity and V is the local electrical potential. The Seebeck effect arises from a local electromotive field,

$E_{emf} = -S\nabla T$, where S is a parameter that depends locally and ∇T is the temperature gradient. The Seebeck coefficient depends strongly on the composition of the material and, in general, also varies with the temperature. The Seebeck coefficient for ordinary materials at room temperature generally lies in the $-100 \mu\text{V/K}$ to $+1,000 \mu\text{V/K}$ range [7-8].

Electrical conductivity (σ) is the measurement of the current carried by a material . It is an intrinsic property of a material and depends on the material properties. The electrical conductivity of a metallic conductor increases progressively as the temperature decreases. Superconductors exhibit a remarkable phenomenon wherein their resistance drops to zero below a critical temperature. Consequently, a current can flow through a superconducting wire loop without the need for applied power. In various systems, conduction is facilitated by either band holes or electrons. In the case of electrolytes, the movement of entire ions takes place, transporting their net electrical charge. For electrolytic solutions, the conductivity of the material is significantly influenced by the concentration of ionic species.

The lattice component of thermal conductivity (k_l) refers to the heat transmission through the vibrations of lattice ions within a solid. Delving into the physics governing the heat conduction process allows for a thorough and nuanced comprehension of the

nature of lattice vibrations in solids. Among a material's fundamental and crucial physical parameters, its thermal conductivity holds significance. It emerges from phonons of all frequencies. Its manipulation has inflicted a huge variety of technical applications that Incorporate the control of temperature in electrical, chemical, mechanical and even nuclear systems materials for thermal barriers and insulation; enhanced thermoelectric materials for increased efficiency; and sensors and transducers[9].

A profound understanding of thermal conductivity proves crucial in the thermal management of diverse systems, including mechanical, electrical, chemical, and nuclear systems. Lattice thermal conductivity plays a key feature in enhancing the ZT values Materials that have ultralow lattice thermal conductivity possess high ZT values, especially two-dimensional materials.

1.2 Two-dimensional Materials

Two-dimensional (2D) semiconductors are highly effective for TE applications and possess exceptional electronic, thermal, optoelectronic, and transport properties, along with quantum confinement effects. 2D materials like graphene, Mxenes (e.g., Ti_4N_3), and allotropes have shown excellent optical and electronic properties, making them incredibly promising for TE use. Apart from these, transition metal dichalcogenides have also shown remarkable results in 2D TE materials. For, a 2D SnSe transistor exhibits a unique value of S and a mobility (μ) of $250 \text{ cm}^2/\text{Vs}$ at 1.3 K [10]. Recent research has focussed on how ZT can be enhanced in monolayers, as seen in materials like MoS_2 , WS_2 , and various other dichalcogenides. Notably, the Mg_3Sb_2 monolayer has shown a favourable ZT of 2.6 at a temperature of 900 K and enhanced ZT values of ≥ 2.5 have been achieved in materials such as PbTe and SnSe [11-12]. Despite significant advancements in both theoretical predictions and experimental measurements, there remains plenty of room to explore better TE performance of different chalcogenides and their derivatives.

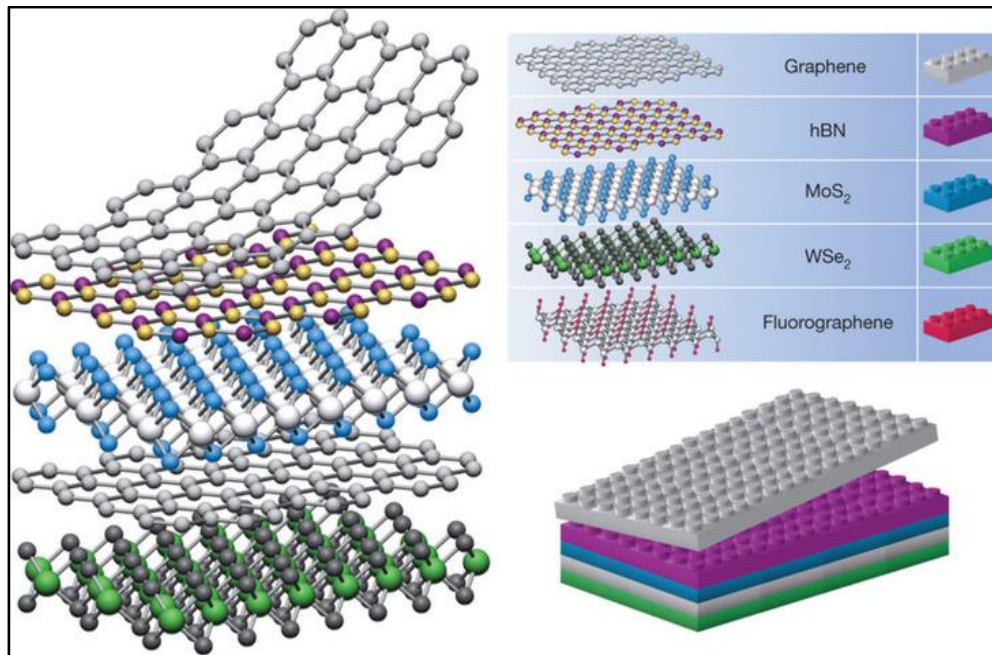


Figure 2: Represents different Two-dimensional Materials (Taken from Geim, A.K., *et al.*, 2013. Van der Waals heterostructures. Nature 499, 419–425.)

One of the prime examples in 2D materials is graphene, **Graphene** consists of a hexagonal lattice of carbon atoms bonded together covalently, forming a structure that's merely one atom thick, approximately 0.14 nanometers in thickness. Being a semimetal, its conduction and valence bands intersect, imparting remarkable properties. Due to its distinctive band structure, electrons traverse through graphene at incredibly high velocities, about 1/300th the speed of light, resulting in exceptional characteristics such as unmatched thermal conductivity. It has shown high ZT values up to 3[13-14].

Phosphorene is also another prime example of 2D materials, they are a single layer of black phosphorus, which is a stable allotrope of phosphorus with a layered structure. It exhibits a honeycomb arrangement which is puckered and serves as a direct bandgap semiconductor. By stacking layers, the bandgap can be adjusted across the visible spectrum. With a charge mobility of approximately $1000 \text{ cm}^2\text{V}^{-1}\text{s}^{-1}$, it is promising for optoelectronics and transistors applications. The corrugated nature of phosphorene

implies that its characteristics can substantially differ depending on the measurement direction within the material [15].

1.3 Bulk materials

Bulk materials have been shown to produce high thermoelectric efficiency due to their high Seebeck coefficients. They show $S^2\sigma$ of approximately $800 \mu\text{W}/(\text{mK})^2$ at 600 K around a doping of 10^{20} cm^{-3} . There have been reports of a variety of bulk materials families that have shown good performance in TE properties. Some of the highly efficient TE materials are low-dimensional that is they are bonded by van der-waall forces while the rest are three-dimensionally bonded. They tend to be highly symmetric as materials with triagonal and cubic symmetry, such as Bi_2Te_3 , SnSe , GeTe , Mg_2Si , PbTe and PtSe_2 , as well as many potential new TE materials. Some examples of families of TE newly uncovered include $\text{Ba}(\text{MgX})_2$ ($\text{X}=\text{P}, \text{As}, \text{Bi}$), X_2YZ_6 ($\text{X}=\text{K}, \text{Rb}, \text{Y}=\text{Pd}, \text{Pt}, \text{Z}=\text{Cl}, \text{Br}$), K_2PtX_2 ($\text{X}=\text{S}, \text{Se}$), i.e. some are materials with zero dimensions with van der Waal interactions along all three axes or along just two axes [16].

other recently found materials for TE advancements are the 3D-bulk materials that have no van-der-waal bonding, such as CaO_2 , K_2PtSe_2 , LiMgN , Al_2ZnS_4 , ZnO_2 , Li_2CuSb etc.

Zintl phases have emerged as promising candidates to fulfil the criterion of TE properties over other conventional materials as the Zintl concept is an excellent way to design new materials with exciting technological applications. Zintl phases are a broad intermetallic compound class with complex crystal structures and intriguing properties like chemical bonding and narrow band gaps. Generally, these compounds consist of cations such as alkali, alkaline earth, or rare earth elements, and an anionic framework that is covalently bonded. Referring to the Zintl-Klemm theory to satisfy the valence requirement. The Zintl compounds like RbZn_4As_3 , EuIn_2As_2 , SrSn_2As_2 , RbGaSb_2 , EuMg_2Bi_2 , Mg_3Sb_2 , YbMg_2Bi_2 , $\text{Ba}_3\text{Cd}_2\text{P}_4$, and $\text{Ba}_2\text{Cd}_2\text{P}_3$ have been synthesized experimentally and theoretically investigated as good thermoelectric materials [17-18].

Heusler compounds are intermetallic compounds with magnetism having FCC structure (face-centred cubic) having a general stoichiometry of XYZ (Half-Heuslers) or X_2YZ (full-Heuslers), where Y and X are transition metals and Z is an element from *p*-block. They have shown high TE performance due to their high tunability. The specific Half-Heusler compounds targeted for thermoelectric applications belong to the space group[19]. These compounds are ternary semiconductors with a general formula XYZ, where X represents a transition metal which have higher electropositivity, such as Ti or Zr, Y denotes a transition metal with lower electropositivity, such as Ni or Co, and Z signifies a heavy main group element, such as Sn or Sb. This broad range of elements enables the formation of various Half-Heusler phases with diverse material properties. Half-Heuslers have a major advantage over other TE materials due to their low level of toxicity, and high thermal and mechanical stability and are excellent candidates for mid-high temperature applications. Many Half-Heuslers have reported showing $ZT > 1$ after reducing the lattice thermal conductivity. Some examples of HH are $MFeSb$ ($M = V, Nb, Ta$), $MCoSb$ ($M = Ti, Zr, Hf$), $MNiSn$ ($M = Ti, Zr, Hf$) etc.[20-22]

Bi_2Te_3 and Bi_2Se_3 , exhibit ZT ranging between 0.8 and 1.0 which are temperature-independent. When these materials are nanostructured to form a superlattice layered structure consisting of alternating Sb_2Te_3 and Bi_2Te_3 layers, they create a device characterized by high electrical conductivity in one direction and low thermal conductivity in the perpendicular direction. This arrangement leads to an improved ZT value, reaching approximately 2.4 at room temperature for the p-type variant [23].

Skutterudites are composed of elements with the composition LM_4X_{12} , in which X signifies a metalloid, typically a group V element like phosphorus, L represents a rare-earth metal, and M denotes a transition metal. These compounds demonstrate a figure-of-merit, ZT , exceeding 1.0 and hold promise for utilization in multistage TE devices. These materials possess blank spaces that can be occupied by ions of low-coordination, typically rare-earth materials. This filling process effectively lowers thermal conductivity by creating additional sources for lattice phonon scattering, while

preserving electrical conductivity. Alternatively, it is feasible to reduce thermal conductivity in skutterudites without filling these voids by employing a unique architecture featuring nano- and micro-pores [24].

Oxide thermoelectric Oxide compounds, exemplified by structures like $(\text{SrTiO}_3)_n(\text{SrO})_m$, known as the Ruddlesden-Popper phase, present layered superlattice configurations, positioning them as favourable options for TE applications at high temperatures. These materials showcase diminished κ perpendicular to the layers while retaining strong electronic conductivity in them. Epitaxial SrTiO_3 films can achieve ZT values of up to 2.4, reflecting their superior thermal stability compared to conventional high-ZT bismuth compounds. NaCo_2O_4 has been noted for its high TE power. Oxides offer various advantages, including low toxicity, high oxidation resistance, and thermal stability. Achieving simultaneous control over the electric and phonon systems may necessitate using nanostructured materials. Layered $\text{Ca}_3\text{Co}_4\text{O}_9$ has demonstrated impressive ZT values ranging from 1.4 -2.6 at 900 K. They are arranged to prevent the stacking of identical atoms on each other, thereby hindering phonon conductivity perpendicular to the layers [25].

CHAPTER 2

METHODOLOGY

2.1. Computational Methods

2.1.1. Density Functional Theory (DFT)

DFT gives us a powerful mathematical tool to analyse the many-body system's electronic properties, including molecules, atoms, and even condensed matter. The theory enables us to determine the properties of such systems based on their spatially dependent electron density, making it a remarkably versatile tool within the field of computational condensed matter physics [26].

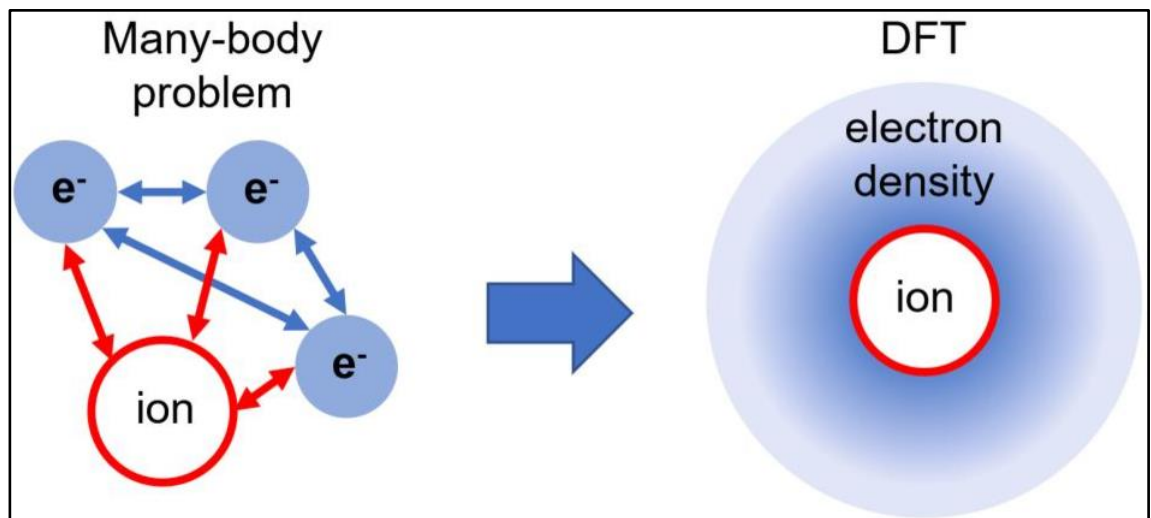


Figure 3: Represents the theme of Density functional theory (Taken from Sergei Posysaev, *et al.*, 2018. Applications of Density Functional theory for modelling semiconductor contacts and calculating oxidation sites. Chemistry, Material Science.)

Derivation and formalism

The Hohenberg-Kohn theorem highlights a main aspect of the function, The electron density that takes part in minimizing the overall functional energy corresponds to the real electron density associated with the complete solution of the Schrödinger

equation. If we were acquainted with the functional form which was accurate, we could adjust the electron density iteratively until the functional's energy is minimized, providing a method for determining the pertinent electron density. In practice, we apply the variational principle using approximate functional forms. Using the Born-Oppenheimer approximation, treated molecule's nuclei or clusters are taken to be stationary, producing a static potential V where electrons are travelling. Then, a wavefunction $\Psi(\mathbf{r}_1, \dots, \mathbf{r}_N)$ meeting the many-electron time-independent Schrödinger equation can be used to describe a stationary electronic state.

$$\hat{H} \Psi = [\hat{T} + \hat{V}_{nu-e} + \hat{V}_{e-e}] \Psi = [\sum_{i=1,2,\dots,N} (-\hbar^2/2m_i) \nabla_i^2 + \sum_{i=1,2,\dots,N} (V_{nu-e}(\mathbf{r}_i)) + \sum_{i<j} V_{e-e}(\mathbf{r}_i, \mathbf{r}_j)] \Psi = E \Psi \quad (1)$$

Where, for the system of N electrons, \hat{H} (Hamiltonian operator), E denotes the overall energy, \hat{T} denotes the kinetic energy operator, \hat{V}_{nu-e} denotes the potential energy operator corresponding to the external field due to the positively charged nuclei and \hat{V}_{e-e} denotes the operator corresponding to inter-electronic interactions. The operators \hat{T} and \hat{V}_{e-e} are identical for any N -electron system and for this reason, are called universal operators. The operator \hat{V}_{nu-e} depends on the specifics of a particular system. Owing to the inter-electronic interaction term corresponding to \hat{V}_{e-e} , The application of DFT allows to mapping of the many-particle problem, containing \hat{V}_{e-e} , to a one-particle problem free from \hat{V}_{e-e} . The electron density $n(\mathbf{r})$, a crucial quantity in DFT, is given for a normalized Ψ by

$$n(\mathbf{r}) = N \int d^3\mathbf{r}_2 \dots \int d^3\mathbf{r}_N \Psi^*(\mathbf{r}, \mathbf{r}_2, \dots, \mathbf{r}_N) \Psi(\mathbf{r}, \mathbf{r}_2, \dots, \mathbf{r}_N) \quad (2)$$

$$\Psi_0 = \Psi[n_0] \quad (3)$$

The fact that the wavefunction is a functional of $n_0(\mathbf{r})$ immediately leads to the finding that the expectation value of an observable \hat{O} when the system is in the ground state is also a functional of $n_0(\mathbf{r})$

$$O[n_0] = \langle \Psi[n_0] | \hat{O} | \Psi[n_0] \rangle \quad (4)$$

Further, it is possible to explicitly write the contributions due to the external potential $\langle \Psi[n_0] | \hat{V}_{nu-e} | \Psi[n_0] \rangle$ as:

$$V_{nu-e}[n_0] = \int V_{nu-e}(\mathbf{r}) n_0(\mathbf{r}) d^3\mathbf{r} \quad (5)$$

This argument can be extended and the contribution due to the external potential may be expressed as:

$$V_{nu-e}[n] = \int V_{nu-e}(\mathbf{r}) n(\mathbf{r}) d^3\mathbf{r} . \quad (6)$$

$T[n]$ and $U[n]$ are referred to as universal functionals, but $V_{nu-e}[n]$ being dependent on the specifics of the given system is referred to as a non-universal functional. Having specified a system, the minimization of the functional

$$E[n] = T[n] + V_{e-e}[n] + \int V_{nu-e}(\mathbf{r}) n(\mathbf{r}) d^3\mathbf{r} \quad (7)$$

The objective is to minimize the energy functional concerning $n(\mathbf{r})$. The minimization process of the energy functional results in the determination of the ground-state electron density ($n(\mathbf{r})$), subsequently determining all other observables associated with the ground state.

The Lagrangian method of multipliers offers a solution to the variational problem of minimizing the energy functional $E[n]$. To initiate the process, we examine an energy functional that does not incorporate the inter-electronic interaction energy.

$$E_{eq}[n] = \langle \Psi_{eq}[n] | \hat{T} + \hat{V}_{eq} | \Psi_{eq}[n] \rangle \quad (8)$$

where \hat{T} denotes the operator corresponding to the kinetic energy, and \hat{V}_{eq} denotes the operator corresponding to the equivalent potential in which the particles are travelling.

E_{eq} can be used to generate the following Kohn-Sham equations for this auxiliary, noninteracting system:

$$[-(\hbar^2/2m) \nabla^2 + V_{eq}(\mathbf{r})] \varphi_i(\mathbf{r}) = \varepsilon_i \varphi_i(\mathbf{r}), \quad (9)$$

which gives the orbitals φ_i that mimic the electron density $n(\mathbf{r})$ of the actual many-particle system

$$N(\mathbf{r}) = \sum_{i=1,2,\dots,n} |\varphi_i(\mathbf{r})|^2 \quad (10)$$

The equivalent single-body potential may be expressed as

$$V_{eq}(\mathbf{r}) = V_{nu-e}(\mathbf{r}) + \int (n(\mathbf{r}')/|\mathbf{r}-\mathbf{r}'|) d^3\mathbf{r}' + V_{EC}[n(\mathbf{r})] \quad (11)$$

first term $V_{nu-e}(\mathbf{r})$ is the extrinsic potential, the second term is the Hartree term expressing the inter-electronic Coulombic interaction, and the third term V_{EC} denotes the exchange-correlation potential. Here the entirety of the many-body interactions is incorporated in the exchange-correlation potential V_{EC} . The task of finding the solution to the KSE is approached in an iterative self-consistent fashion. Initially, a starting guess for $n(\mathbf{r})$ is made following which the corresponding V_{eq} is determined and the Kohn-Sham equations are solved for the φ_i . Using these φ_i 's a new electron density is determined and the aforementioned sequence of steps is repeated. Up until convergence, this process is repeated [27].

2.1.2. Exchange correlation functional

It is guaranteed that the exchange-correlation functional has a correct shape by the Hohenberg-Kohn theorem, which remains unknown. However, there is a specific scenario in which we can precisely derive this functional: the uniform electron gas. In this instance, we assume that the $n(\mathbf{r})$ remains the same at all points in space, denoted, $n(\mathbf{r}) = 1/4$ constant. While this seems limited in relevance to real materials, which exhibit variations in electron density defining chemical bonds and contributing to material

properties, the uniform electron gas offers a practical means to apply the KSE. Using this method, the known exchange-correlation potential from the uniform electron gas at the electron density observed at that place is set at each position.. This is accomplished by analysing the same system employed in the KSE. Through the K-S formulation of DFT, the total energy is expressed as follows

$$E_{tot, KS-DFT} = \sum_i \int \Psi_i^*(\mathbf{r}) \nabla^2 \Psi_i(\mathbf{r}) d^3\mathbf{r} - \sum_J \int (Z_J/|\mathbf{r}-\mathbf{R}_J|) n(\mathbf{r}) d^3\mathbf{r} + \frac{1}{2} \iint (n(\mathbf{r})n(\mathbf{r}')/|\mathbf{r}-\mathbf{r}'|) d^3\mathbf{r}d^3\mathbf{r}' + E_{EC} + \frac{1}{2} \sum_{I \neq J} (Z_I Z_J / |\mathbf{R}_I - \mathbf{R}_J|) \quad (12)$$

The first right-hand term side expresses the electronic non-interacting kinetic energy, the next term expresses the nuclei-electron interaction energy followed by the Coulombic inter-electronic interaction energy, the next term expresses the exchange-correlation energy and the fifth term expresses the inter-nuclei interaction energy. The orbitals and the electron density $n = \sum |\Psi_i|^2$ are attained by self-consistently solving the Kohn-Sham equations: Self-consistently solving KSE yields the orbitals Ψ_i and the electron density $n = \sum |\Psi_i|^2$ that may be used for the determination of $E_{tot, KS-DFT}$:

$$(-\frac{1}{2}) \nabla^2 - \sum_J (Z_J / |\mathbf{r}-\mathbf{R}_J|) + \int (n(\mathbf{r}')/|\mathbf{r}-\mathbf{r}'|) d^3\mathbf{r}' + v_{EC}(\mathbf{r}) \Psi_i(\mathbf{r}) = \varepsilon_i \Psi_i(\mathbf{r}) \quad (13)$$

The exchange-correlation energy functional E_{EC} and potential $v_{EC} = \delta E_{EC} / \delta n$ are the only terms in $E_{tot, KS-DFT}$, and the Kohn-Sham equations that are not precisely known. As a result, the correctness of the estimated characteristics is primarily dependent on the E_{EC} and v_{EC} estimates. A multitude of exchange and correlation approximations have been developed. They can be divided into several categories, including GGA, LDA, meta-generalized gradient approximation (meta-GGA), and hybrid approximations [28].

2.1.3. Generalised gradient approximation

When the correlation functional was expanded in terms of the gradient of the density through the Taylor series and terminated it at some order. Such an approximation is known as gradient expansion approximation (GEA), this was initiated by Herman in 1969. It turned out that such an approximation often gave worse results and did not provide any improvement over local density approximations. This was because the gradients of the density in the real system become very large; as a result, such expansions break down. It was also found that the GEA does not satisfy most of the sum rules. Later only, it was realized that there was no need of such an expansion and it was possible to construct exchange-correlation functional, which was a functional of density as well as its gradient and satisfied the sum rules. This could be written as [29]

$$E_{xc} [n_{\uparrow}, n_{\downarrow}] = \int d^3 r f(n_{\uparrow}(r), n_{\downarrow}(r), \nabla n_{\uparrow}, \nabla n_{\downarrow}) \quad (14)$$

2.1.4. The LAPW method -

The LAPW method is one of the most precise methods for finding crystal electrical structures. It is based on DFT and addresses exchange and correlation using approaches such as the local spin density approximation (LSDA). There are several types of LSDA potentials, and new advancements employing the generalized gradient approximation (GGA) are also available. On either a scalar or a vector relativistic method, relativistic effects in valence states can be incorporated. or a second variational technique that takes spin-orbit coupling into account. The core states are treated in their entirety relativistically.

2.1.5. Boltzmann Transport Theory

The Boltzmann transport theory expresses the interplay between the driving effect of the extrinsic fields and the dissipative effect of scattering of carriers by phonons and defects. This theory can be used to explore how the thermal equilibrium distribution

of carriers changes in the presence of external forces and electron scattering mechanisms.

The Boltzmann equation, which is presented below, serves as the foundation for the analysis of solid-state transport characteristics.

$$\partial f / \partial t + v \cdot \nabla_r f - (e / \hbar) \varepsilon \cdot \nabla_k f = (\partial f / \partial t)_s \quad (15)$$

The drift terms are on the left-hand side and the terms on the right are scattering term. Let us assume that these scattering processes are immediate and can change the electron's local state from k to k' . Define $W(k, k')$ as the scattering rate between the k and k' states. If k' is empty and k state is filled. The rate at which scattering alters the distribution function $f_k(v)$ is

$$(\partial f(\mathbf{r}, \mathbf{k}, t) / \partial t)_s = (V / (2\pi)^3) \int d\mathbf{k}' \{ [1 - f(\mathbf{r}, \mathbf{k}, t)] W_{k'k} f(\mathbf{r}, \mathbf{k}', t) - [1 - f(\mathbf{r}, \mathbf{k}', t)] W_{k'k} f(\mathbf{r}, \mathbf{k}, t) \} \quad (16)$$

the $2\pi^3$ denominator originates from the count of permissible states within a k -space d^3k' . In the integral, the initial term signifies the electron rate transition from ' k' ' state (hence the factor ' $f_{k'}$ ') to k which is unoccupied hence the factor $(1 - f_k)$. The subsequent term accounts for the loss aspect. In a state of steady equilibrium, there is no alteration in the $f_k(v)$, and the overall summation of the partial derivative terms remains constant.

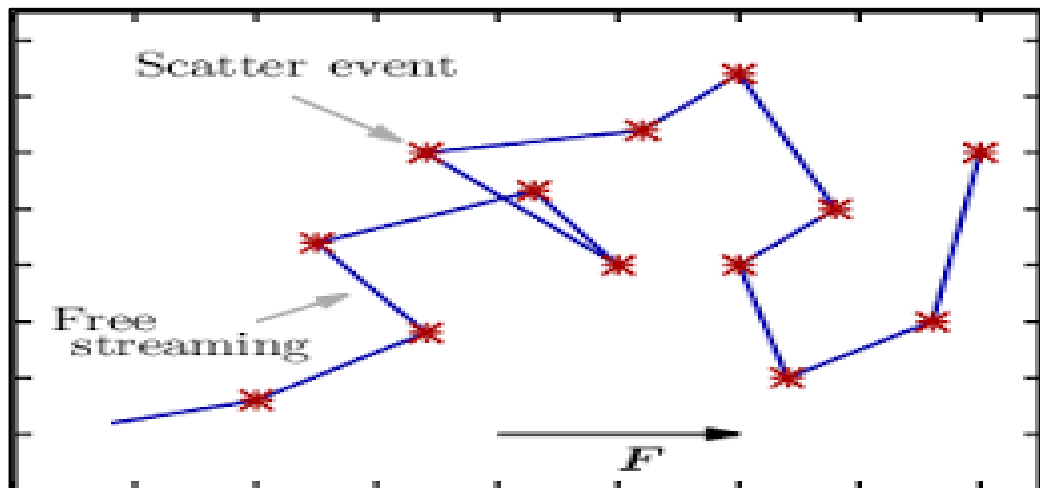


Figure 4: Scattering of particles in a crystal structure (Taken from Markus Bina..., *et al.*, 1985. Charge Transport Models for Reliability Engineering of Semiconductor Devices.)

2.2. Computer programs

2.2.1 VASP

The Vienna Ab Initio Simulation Package (VASP), is a tool employed for conducting quantum mechanical calculations. This involves the use of PAW, coupled with a plane wave basis set. VASP solves the many-body Schrödinger equation approximately by solving the KSE (in the framework of DFT) or by solving the Roothaan equations (in the framework of the Hartree-Fock approach). Additionally, certain hybrid functionals that inherit aspects from both the Hartree-Fock approach and the DFT are also available. VASP calculates key quantities through plane wave basis: single-electron orbitals, charge density, and local potential. The exchange the electrons and ions is either expressed with the help of the PAW method or with the help of norm-conserving or ultrasoft pseudopotentials[30].

VASP carrier out calculations using 4 necessary input files, which are

1. **INCAR:** This file is used to determine what kind of calculation has to be done on the investigated system There are certain tags specified in the INCAR file which we have to set to select a certain algorithm and set the parameters.
2. **POSCAR:** this file gives the details of the system that we study. it consists of the atomic positions in the unit cell and the translational vectors.
3. **POTCAR:** This file consists of the pseudopotential for every single atomic species which is present in Mendeleev's
4. **KPOINTS:** This file sets the mapping for the irreducible Brillouin zone in the crystal reciprocal lattice structure

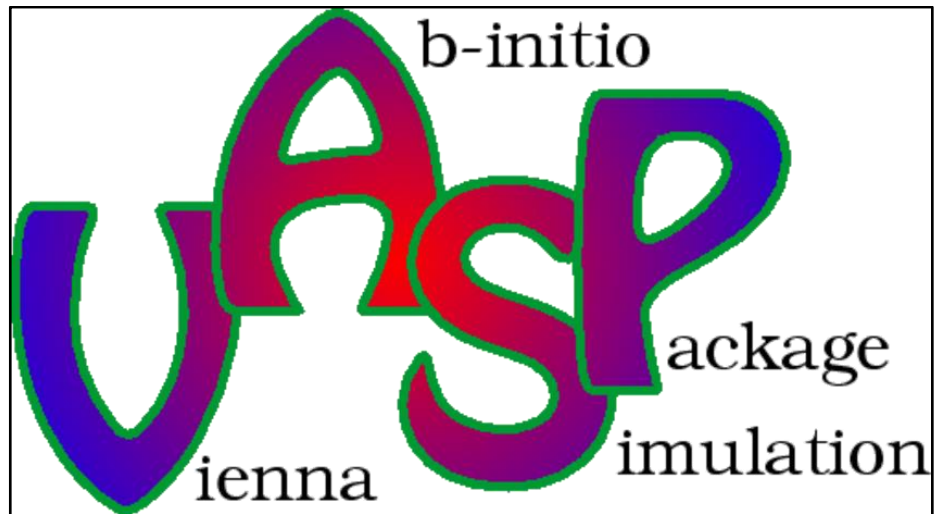


Figure 5: The Logo of VASP

2.2.2 WIEN2k

WIEN2k is a program designed to calculate the electronic structure of solids DFT. It utilizes the most precise methods for determining band structure: local orbitals (Lo) combined with the full-potential LAPW method. WIEN2k is an all-electron system that includes several features and accounts for relativistic effects.

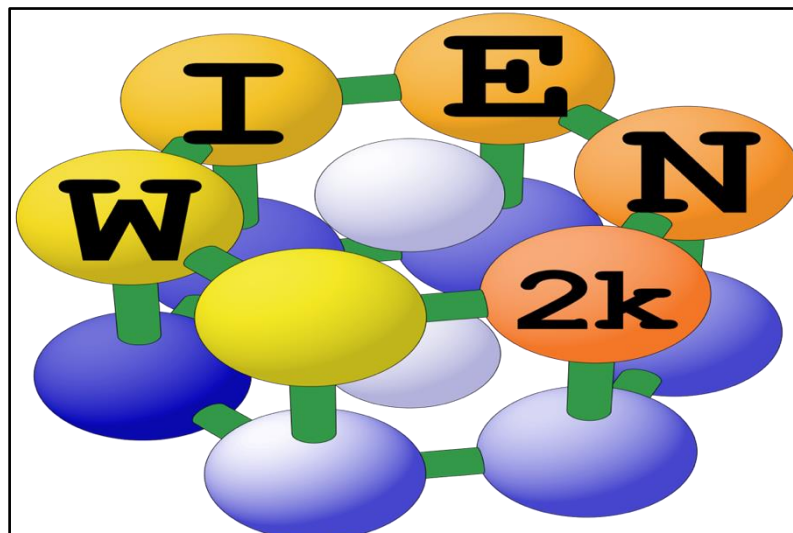


Figure 6: The logo of WIEN2k software

2.2.3 BoltZTraP2

BoltZTraP2 is a software that utilises the linearized BTE to determine smoothed Periodic function Fourier expressions and their accompanying transport coefficients for extended systems. It utilizes the band structure,

The program may be used as a Python module or through a command-line interface.

One of the most important merits of the procedure employed by BoltZTraP2 is the computational ease in the evaluation of transport coefficients due to its ability to efficiently compute group velocities of quasi-particles.

BoltZTraP is frequently used in conjunction with the CRTA. Within the CRTA, the S becomes independent of the scattering rate. As a result, it is possible to obtain the Seebeck coefficient. The combination of CRTA and RBA makes the group velocities independent of μ and T which also proves to be computationally advantageous as it removes dependence of the transport distribution function from temperature and doping. A single scan over a fixed transport distribution function can be used for the evaluation of the dependence of the transport coefficients on temperature and doping. The Fermi distribution function is solely responsible for the temperature and doping dependency of the transport coefficients.: E.g., only σ and κ_e dependent on τ are delivered by it [31]

2.2.4 AMSET

The AMSET code stands for ab initio scattering and transport method which uses the electronic Boltzmann transport equation (BTE) to calculate rates of scattering and mobilities using the Born approximation. The code takes into consideration of various scatterings like acoustic deformation potential (ADP), ionized impurity scattering (IMP), and polar optical phonon scattering (POP) which are the most common scattering types found in semiconductor-like materials. The ADP is responsible for the electron-phonon interactions. IMP represents the charge carriers scattering through the ionization of lattice, and POP includes the exchange of electrons and polar optical phonons. Matthiessen's rule can find out the resultant carrier relaxation time, the inverse of scattering rates by the following equation [32]:

$$\frac{1}{\tau} = \frac{1}{\tau_{ADP}} + \frac{1}{\tau_{IMP}} + \frac{1}{\tau_{POP}} \quad (17)$$

Where τ_{ADP} , τ_{POP} , τ_{IMP} are the time of relaxation from the ADP, POP and IMP scattering. In ADP and IMP scatterings, electrons undergo elastic scattering, where they neither gain nor lose energy. On the other hand, POP scatterings show inelastic scattering behaviour characterized by phonon emission or absorption-induced energy changes. The Fermi golden rule is applied to compute both elastic and inelastic scattering rates. This rule allows us to calculate the transition rates from an initial quantum state $n\mathbf{k}$ to a quantum state $m\mathbf{k} + \mathbf{q}$.

$$\tilde{\tau}_{nk \rightarrow mk+q}^{-1} = \frac{2\pi}{\hbar} |g_{nm}(k, q)|^2 \delta(\varepsilon_{nk} - \varepsilon_{mk+q}) \quad (18)$$

\hbar stands for Planck's constant, δ represents a Dirac delta function, and n relates to the Bose-Einstein distribution. The quantity ε_{nk} pertains to the energy of the state $|n\mathbf{k}\rangle$, while $g_{nm}(k, q)$ signifies the coupling matrix element governing the specific scattering process under consideration. To attain the scattering rates, it is necessary to have deformation, static and high-frequency constants along with elastic constants and dense and uniform band structures.



Figure 7: The Logo of AMSET

CHAPTER 3

LITERATURE SURVEY

3.1 Survey for AgSbS₂ monolayer

2D materials like graphene, MXenes (e.g., Ti₄N₃), and allotropes have shown excellent optical and electronic properties, making them incredibly promising for TE use. Apart from these, transition metal dichalcogenides have also shown remarkable results in 2D TE materials.

Graphene

- In its pure form, graphene does not present itself as a favourable TE material, primarily due to its exceptionally high phonon thermal conductivity. Nevertheless, studies have revealed that graphene is exceptionally versatile in terms of its thermoelectric properties. It can be nanostructured to fine-tune its performance across a wide spectrum, ranging from low to exceptionally high thermoelectric capabilities.
- Finite size effects can induce a bandgap opening in graphene nanoribbons (GNRs), resulting in larger Seebeck coefficients and higher Z-T values compared to 2D sheets [33]. Ouyang and Guo were the first to investigate thermoelectricity in ribbons in 2009 [34].
- Strongly reduced thermal conductance enabled ZT values of up to 3.25 at 800K and around 2 at room temperature in chevron-type graphene ribbons doped with ¹⁴C isotope.

MXene

- MXenes refer to a class of two-dimensional transitional metal carbides or nitrides. Since it discovered Ti_3C_2 in 2011, the MXene family has undergone diverse advancements. The MAX phases have a chemical composition denoted as $\text{M}_{n+1}\text{AX}_n$, with n ranging from 1 to 3. These MAX phases are layered materials with metallic properties, where A represents primarily group 14 and 13 elements of the periodic table, X denotes carbon or nitrogen, and M is for early transition metals such as Zr, Sc, Hf, Ta, Mo, Hf, Ti, V, Nb, etc[35].
- The exceptional electric conductivity, superior chemical and structural stabilities, high hydrophilicity, and superb surface chemistry of the MXenes sustain a strong commitment to renewable energy applications. The intrinsic 2D layered structure of MXenes and the flexibility of its potential surface termination groups present excellent chances to modify the thermal and electronic properties in a way that is advantageous for TE applications. Further benefits for applications in wearable electronics are provided by MXenes' superior mechanical flexibility when compared to many TE materials[36].

Group IVA–VIA Compounds

The compounds in group IVA–VIA are the most promising bulk thermoelectric materials, and significant advancements have been made in this field recently. Reducing the dimensionality of materials boosts their ZT values by increasing the DOS near the Fermi level, leading to a higher Seebeck coefficient. Two particularly effective techniques for tuning the thermoelectric properties of these materials are strain engineering and heterostructure [37].

TMDC(transition metal dichalcogenides)

- The noteworthy chemical stability, advantageous mechanical and physical properties, and adjustable semiconducting characteristics of two-dimensional transition metal dichalcogenides (2D TMDCs), including MX_2 ($X = \text{S, Se, Te}$) and $M = \text{Mo, W, Ti}$, have garnered considerable attention in recent years. These materials exhibit potential for high-performance TE devices. This makes them particularly promising for the advancement of power generators and wearable heating/cooling devices. In comparison to graphene, 2D TMDCs showcase a lower thermal conductivity, further enhancing their suitability for thermoelectric applications[38].
- Theoretical studies suggest that variations in layer number have a minimal impact on the Seebeck coefficients of TMDCs. However, there is a noticeable difference in electrical conductivity based on layer thickness. This provides an opportunity to optimize thermoelectric efficiency by tailoring the layer thickness.

Silver based dichalcogenides

- Silver-based chalcogenides have garnered significant interest as promising TE materials operating at or near room temperature. These materials are expected to drive substantial advancements in energy harvesting for self-powered wearable medical systems and intelligent devices. Compounds like Ag_2E (where $E = \text{S, Se, Te}$) and their other derivatives and hybrids are particularly noteworthy for these applications [39].
- Generally, these materials exhibit compelling attributes due to their high electron mobility, lower electron effective mass, and very narrow band gap contributing to high σ . Consequently, they have ZT values ranging from 0.6 to 1.1 across different temperature ranges. Particularly, Ag_2S has a low σ value of

the order 10^{-1} Sm^{-1} , a low S , and an appreciably high κ_e value; these parameters resulted in constrained TE performance [40].

- efforts have been made to maximise the carrier concentration of Ag_2S by preparing nonstoichiometric Ag_{2-x}S through Ag vacancies, which enhanced the TE properties and stopped the reduction of sulphur atoms, which were volatile through sublimation [41].

3.1.1 . selection of a suitable silver-based dichalcogenide

Suitable Silver bases dichalcogenide

- An abundance of Sb is anticipated to generate Sb_2Te_3 impurities, fostering high-concentration boundary interfaces within the material. Consequently, this scenario is poised to lower κ_1 by intensifying phonon scattering at these interfaces. This phenomenon is beneficial for thermoelectric applications because it enhances the material's ability to convert temperature gradients into electricity. Lower κ_1 minimizes heat transfer through the material, allowing for better thermoelectric efficiency[42].
- A $\sim 0.5\%$ Sb-doping is found to enhance the hole concentration from $\sim 10^{18} \text{ cm}^{-3}$. I-V-VI₂ semiconductor group, in which I=Cu or Ag, V= Sb or Bi, VI = chalcogens (S, Se or Te), are found to be promising TE materials due to their intrinsically low κ_1 . ZT values of $\text{Ag}_{1+x}\text{Sb}_{1-x}\text{Se}_2$ ($x = 0.00, 0.01, 0.02, 0.03$) Due to the combined effect of high $S^2\sigma$ and lowered κ_1 , a ZT value of ~ 1.02 was achieved for $\text{Ag}_{1.02}\text{Sb}_{0.98}\text{Se}_2$ at 673 K[43].
- for this study we considered a derivative of the CuMN_2 (M=Bi, Sb N=S, Se) family in their monolayers . this group has shown optimal ZT values ranging from 0.70-1.50 for n-type and 0.90-1.17 for p-type at 300 K through carrier concentration optimization, which is higher or somewhat similar to many 2D TE materials such as PdSe (0.9) and InSe(0.5). due to their significantly low

lattice thermal conductivity. CuSbS_2 which has an orthorhombic phase was considered as our base structure having a considerably well band gap of 1.10 eV and a ZT value of almost 1.17 [44].

- we considered the iso-structure of cusbs_2 i.e. AgSbS_2 which is a silver-based chalcogenide derived from the CUMN_2 family. AgSbS_2 exhibits a rectangular phase with two-fold rotations and orthogonal mirror planes. AgSbS_2 nanofilms have been made with Ag-dibutyl dithiocarbonate complex in DMF and Sb-butyl dithiocarbonate complex. AgSbS_2 have shown potential for solar cell application due to its high absorption coefficient ($\alpha=10^5 \text{ cm}^{-1}$) [45].

3.2 Survey of KCd_4P_3

Half-Heusler

- Half-Heusler (HH) alloys, along with other semiconducting materials, have recently demonstrated significant potential as TE materials. These materials are composed of lightweight, and environmentally friendly elements. They are thermos-resistant at high temperatures and have intrinsically high power factors[46].
- The composition of HH alloys is typically XYZ, where Z is a major group element and X and Y are transition metals. These alloys are classified as space group F-43m and have the MgAgAs structural type, with four different face-centered cubic (fcc) sublattices making up their structure.
- A significant portion of thermoelectric works has concentrated on HH alloys with compositions of MCoSb and MNiSn , in which M represents Ti, Zr, or Hf. whereas, more recently, other HH alloys like $(\text{V}, \text{Nb})\text{FeSb}$, as well as a

full-Heusler alloy, VFe_2Al , have emerged as promising candidates for TE devices.

- Their applications in spintronics, magnetoelectric, magnetocaloric and ferromagnetic shape memory alloys have highlighted the importance of these materials. Among the Heusler alloys, equiatomic Quaternary Heusler alloys (EQH) stand out as one of the most significant groups. Their low power dissipation and crystallization in the Y-structure make EQH alloys more suitable for a wide range of applications compared to other HAs. Heusler alloys can be categorized based on their stoichiometry into three types: (i) equiatomic Half-Heusler (XYZ), and (ii) 2:1:1 full-Heusler (X_2YZ).
- $ZrFeTiZ$ ($Z= Si, Ge, Al$), $ZrFeTiZ$ ($Z= In, Al, Ge$), and $ZrCoTiZ$ ($Z= Al, Ga, Si, Ge$), have been studied for spin-gapless semiconductors. [47].

Zintl

- Zintl phases are a broad intermetallic compound class with complex crystal structures and intriguing properties like chemical bonding and narrow band gaps. Generally, these compounds consist of cations such as alkali, alkaline earth, or rare earth elements, and an anionic framework that is covalently bonded. Referring to the Zintl-Klemm theory to satisfy the valence requirement
- The Zintl compounds like $RbZn_4As_3$, Mg_3Sb_2 , $YbMg_2Bi_2$, $Ba_3Cd_2P_4$, and $Ba_2Cd_2P_3$ have been synthesized experimentally and theoretically investigated as good thermoelectric materials. Zintl compounds have been studied in past. In the past years Zintl phases have emerged as promising candidates to fulfil the criterion of TE properties over other conventional materials as the Zintl concept is an excellent way to design new materials with exciting technological applications

- RbZn₄As₃ exhibits a remarkably high S of approximately 800 μVK^{-1} and high resistivity at room temperature. The Zintl phase Mg₃Sb₂ has shown remarkable growth in its TE performance by the application of biaxial strain that enabled the tuning of band structure so that the band degeneracy of the valence and conduction band increases, leading to an increase in the value of S and power factor, hence, producing a ZT value of 2.6 around -2.5% strain at room temperature.
- In the calcium-doped Zintl phase, EuMg₂Bi₂ with strain fluctuations in misfit dislocations in the grain boundary showed a high rise in the S and κ yielded a high ZT value of 1.3 [48-52]

3.2.1 Selection of a suitable Zintl compound

- Complex structure pnictides, particularly I-II₄-V₃ (I = alkali metal; II = divalent transition metal; V = pnictide element) compounds show structural chemistry. Pnictide compounds attract significant amount of attention due to their richness in structural chemistry, unique optoelectronic and catalytic properties.
- They can be considered as a potential candidate in the field of superconductivity, thermoelectricity and optical applications like infrared detection and lasing action. These phases exist in orthorhombic($Pnma$), monoclinic(Cm), rhombohedral($R\bar{3}m$) and tetragonal($P4/mmm$).
- The ACd₄Pn₃ phase (A = Na, K, Rb) (Pn = P, As) has been previously synthesised and crystallised in the polymorphs. The synthesis study of NaCd₄P₃ showed higher stability in $R\bar{3}m$ and Cm structures as they had low total energy differing by 30 meV and lower than the rest of the structures[53].

- KCd_4P_3 an isostructural of NaCd_4P_3 is experimentally synthesized by rapidly cooling stoichiometric mixtures of the respective elements in a 1:4:3 ratio, typically after homogenization at elevated temperatures, such as between 700 and 850 degrees Celsius[54]. For this work, we study the TE and electronic properties of KCd_4P_3 by employing first-principles calculations in connection with BTE with CRTA and RBA.

3.3 Motivation

The ever-increasing global demand for clean and sustainable energy necessitates the exploration of novel and efficient energy harvesting technologies. Thermoelectric energy harvesting offers a promising solution by converting waste heat into electricity, contributing to a more sustainable energy future. 2D and 3D materials, with their unique electronic, thermal, and mechanical properties, have emerged as potential candidates for high-performance thermoelectric materials due to their exceptional tunability. This research project delves into the potential of 2D and 3D materials as a game-changer in thermoelectric energy harvesting. So our major aim is to follow these main objectives.

- To explore the capacity of these materials to transform discarded thermal energy into usable electrical power.
- to delve deeper into ZT properties of emerging and novel two-dimensional materials, using particularly first-principles calculations.
- To create and improve new configurations and compositions of 2D and 3D materials to increase their ZT by examination of various techniques such as doping strategies and strain engineering.

CHAPTER 4

RESULTS AND DISCUSSION

4.1 Results and discussion for AgSbS₂ monolayer

4.1.1 Structural properties

This study focused on AgSbS₂ in its orthorhombic phase which is characterised by the space group *Pnma* (No. 62). Within this structure, Ag¹⁺ ions are coordinated with four S²⁻ ions, forming AgS₄ tetrahedra that share corners with eight identical SbS₅ square pyramids and also share corners with other four identical AgS₄ tetrahedra, along with one SbS₅ square pyramid. The structural optimization of the bulk AgSbS₂ was performed and then the resultant optimised structure was further used to obtain its monolayer. AgSbS₂ monolayer exhibits a rectangular phase where Ag is bonded with three Sb atoms and three S atoms as depicted in Figure 8, characterized by two-fold rotations and orthogonal mirror planes. The optimized lattice parameters for the monolayer of this compound in its equilibrium state were obtained and listed in Table 1. So far, no previous studies of the investigated structure have been done, therefore, we have compared its structural parameters to its iso-structure CuSbS₂. In addition, the crystal structure shows anisotropic properties, making it applicable for tuneable structural, elastic and transport properties that might help to improve TE performance.

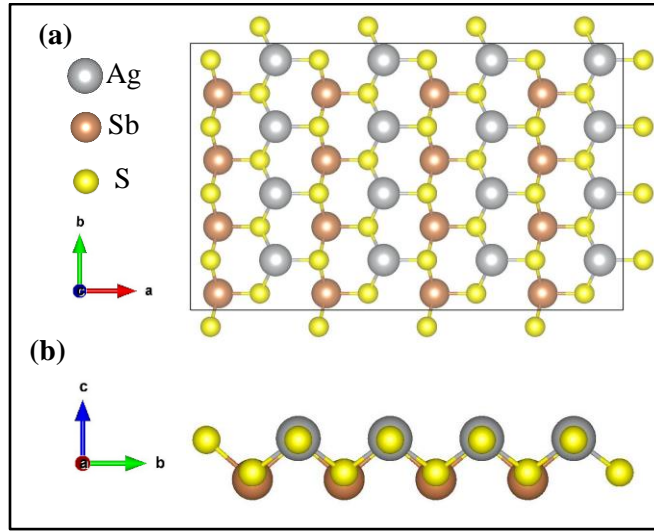


Figure 8: Top view of the monolayer structure of AgSbS₂ b) The side view of the monolayer structure of AgSbS₂

Table 1 Obtained structural parameters (a and b in Å and V in Å³) and bond lengths (in Å) of AgSbS₂ in comparison with its iso-structure CuSbS₂

Material	Structural parameters			Bond lengths	
	a	b	V	Ag/Cu-S ₁	Sb-S ₁
AgSbS ₂	6.367	3.927	390.403	2.327	2.435
CuSbS ₂ [44]	6.15	3.81	338.226	2.308	2.484

4.1.2 Computational details

The structural, elastic, and electronic properties of a monolayer of AgSbS₂ were assessed using DFT within VASP, employing the PAW method. A vacuum of 10 Å is added in the c -direction for a further set of calculations. PBE-GGA was utilized for structural optimization where the Kohn-Sham equations were solved self consistently till meeting a convergence criterion of $10^{-6}/\text{Å}$. The Γ -centred sampling scheme with k -point mesh grid of size $11 \times 11 \times 1$. A plane wave cutoff of 450 eV, validated through energy optimization compass self-consistent field calculations using both PBE and the

Heyd-Scuseria-Ernzerhof hybrid functional (HSE06) [55]. The hybrid functional helps to compute E_g more accurately. The transport properties were using the AMSET code. This work considered the ADP, IMP and POP which are the most common scattering types found in semiconductor-like materials. To attain the scattering rates, it is necessary to have deformation, static and high-frequency constants along with elastic constants and dense and uniform band structures. In our calculations, these are all obtained using DFT and density functional perturbation theory (DFPT). The average relaxation time is calculated from all the scattering rates and is incorporated by the code to find the transport parameters S , σ , and κ_e by solving BTE using an interpolation factor of 10.

4.1.3 Stability Analysis

It is necessary to assess the stability of the studied monolayer before doing further calculations as it is not experimentally realized yet. The monolayer has been confirmed to meet the thermodynamic stability criteria by calculating the cohesive energy (E_{coh}) through the following equation [56]:

$$E_{coh} = \left[E_{AgSbS_2} - (E_{Ag} - E_{Sb} - 2E_S) \right] / N \quad (19)$$

The ground state energy (E_{AgSbS_2}) of AgSbS₂ can be expressed as a function of the total number of atoms in its unit cell (N) and the individual total energy per atom for Ag, Sb, and S in their respective bulk states (E_{Ag} , and E_S). The calculated E_{coh} for the AgSbS₂ monolayer was determined to be -6.868 eV/atom, hence confirming it is thermodynamically stable.

The elastic constants were evaluated by the energy strain relationship to ascertain the mechanical stability. Since, the monolayer forms a rectangular structure, it possesses four independent elastic constants, C_{11} , C_{12} , C_{22} and C_{66} where $C_{11}=11.057$, $C_{12}=1.801$, $C_{22}=15.252$ and $C_{66} = 2.533$, all in units of Nm⁻¹. The Born stability criteria for this structure is given as:

$$C_{11} * C_{22} > C_{12} * C_{12} \quad C_{11} > 0, \quad C_{66} > 0 \quad (20)$$

All the stability criteria for the rectangular structure were met, suggesting that the rectangular form remains mechanically stable in regular ambient conditions.

The Young's modulus (Y), bulk modulus (B), shear modulus (G), and Poisson's ratio (ν) were found to infer various mechanical properties such as brittleness, ductility stiffness, and strength of AgSbS₂ monolayer. The values of the elastic constants are presented in Table 2. The values of B and G were approximated using Voigt-Reuss hill approximation. B dominates the mechanical stability as it has a higher value than G . The Pugh ratio (B/G) is higher than 1.75, which shows the ductile nature of AgSbS₂. The anisotropy in AgSbS₂ results in a ν of approximately 0.118 along a -direction the ν and 0.484 along the b -direction. ν serves as an indicator of the bonding characteristics of the material. When the Poisson ratio falls within the range of 0.25 to 0.5 [57-59], it suggests the prevalence of central forces in the material's bonding. In the case of the AgSbS₂ monolayer, the presence of central forces found to be present along the b -direction and a presence of noncentral forces along the a -direction which signifies a covalent nature in a -direction. These elastic constants were used to determine the Debye temperature (θ_D) using following expression:

$$\theta_D = (h/k_B) \left[\left(\frac{3n}{4\pi} \right) (N_A \rho / M) \right]^{\frac{1}{3}} \cdot v_m \quad (21)$$

Where ρ is the density, N_A is the Avogadro number, k_B is the Boltzmann constant, n is the number of atoms in the monolayer, M is the molecular weight of the compound, and is the average sound velocity. The longitudinal (v_l) and transversal (v_t) sound both contribute to the average sound velocity (v_m) by using elastic constants through the following equations [60]:

$$v_m = \left[\frac{1}{3} \left(\frac{2}{v_t^3} + \frac{1}{v_l^3} \right) \right]^{-\frac{1}{3}} \quad (22)$$

$$v_l = \sqrt{\frac{G}{\rho}} \quad (23)$$

$$v_t = \sqrt{\frac{3B+4G}{\rho}} \quad (24)$$

By solving these equations, we got the values of v_t , v_m , v_l , and θ_D along both directions as presented in Table 2. The maximum values of Y , v and θ_D of CuSbS₂ were 66.53 Nm⁻¹, 0.14 and 90.10 K respectively. The maximum value Y for AgSbS₂ was found to be much lower than CuSbS₂, hence resulting in a comparatively higher value Debye temperature.

Table 2 Obtained Young's Modulus (Y), Bulk Modulus (B), Shear Modulus (G) in Nm⁻¹, the transverse (v_t) and longitudinal (v_l) sound velocity, mean sound velocity (v_m) in Kms⁻¹ and Debye temperature (θ_D) in K of AgSbS₂.

Direction	Y	B	G	v	v_t	v_l	v_m	θ_D
a -direction	7.518	7.478	2.553	0.118	1.93	0.54	0.767	114
b -direction	14.958	7.478	5.530	0.484	2.93	0.796	0.892	132.29

4.1.4 Electronic Structure

The band structure and the DOS are essential parameters that give us information about the electronic and transport properties. The band structure was calculated using both PBE and HSE06 functionals as depicted in Figure 9. Even though the band gap values calculated by both methods differ, the behaviour of the electronic band remains the

same. We identified AgSbS₂ as a semiconductor with indirect band gap as the top of its VB is located at Γ and the bottom of the conduction band CB is located at X. The E_g values of 0.58 eV using PBE and 1.31 eV using HSE06 are estimated which turned out to be comparable to the other ternary and binary dichalcogenides monolayers like CuSbS₂ (1.10 eV), CuBiS₂ (0.83 eV) and SnSe₂ (0.715 eV) that are well known for their TE performance. For VB maxima the deformation potential (E_l) has a value of 3.53 eV along the a -direction and 5.25 eV along the b -direction, whereas for the CBM, it is 0.89 eV along the a -direction and 4.59 eV along the b -direction. The carrier mobility increases when E_l is large, conversely, it may decrease if the deformation potential attains lower values [61].

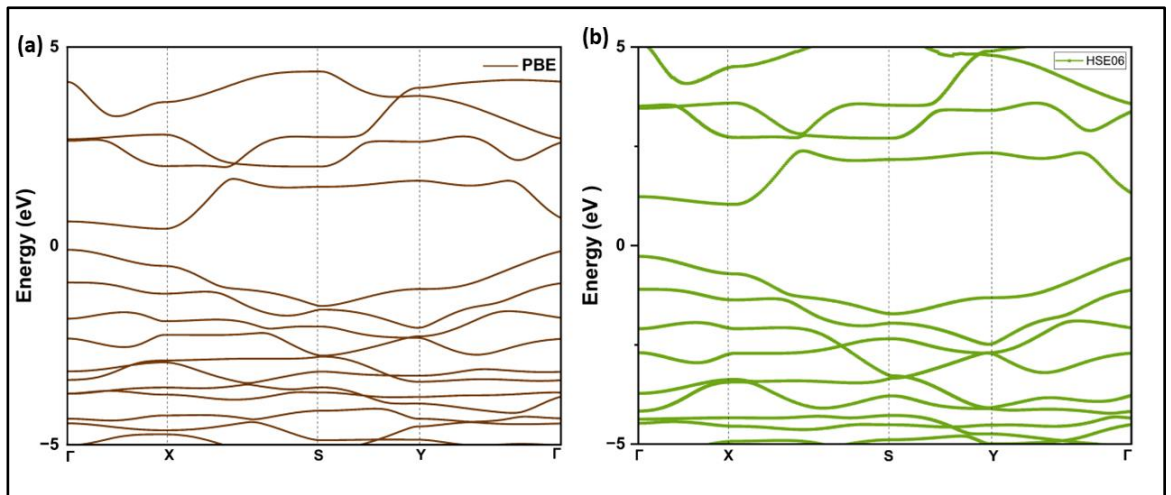


Figure 9: Electronic band structure of AgSbS₂ (a) using PBE (b) using HSE06

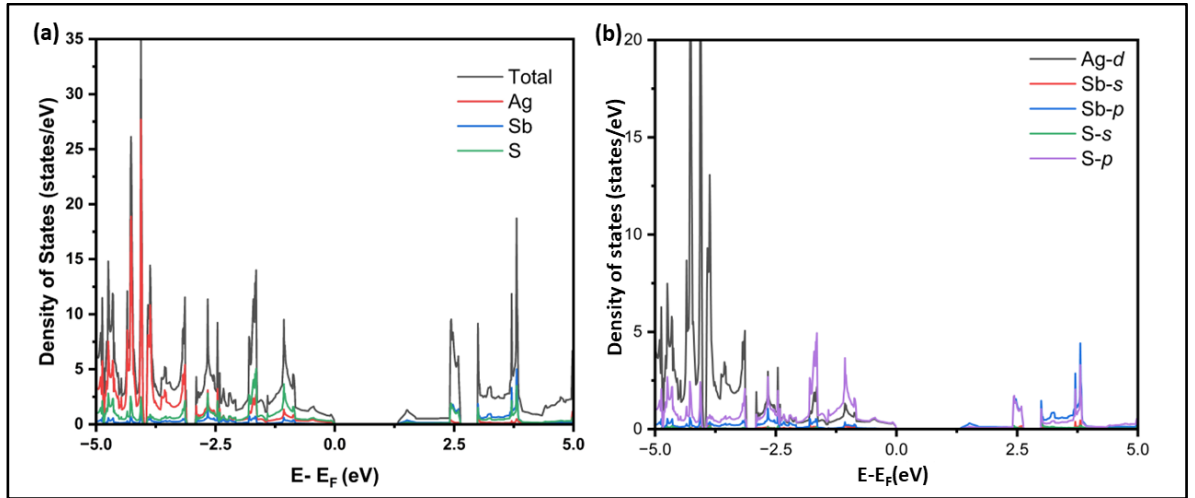


Figure 10: (a)The total Density of States(b)The partial Density of States of AgSbS₂ using HSE06 functional

The analysis of the DOS using HSE06 functional, as shown in Figure 10(a) reveals that the lower states in the VB (from -5 eV to -2 eV) are primarily occupied by the Ag atoms. The top of the VB (from -2 eV to -0.5 eV) has a major contribution of S atoms and a negligible contribution from Sb. On the other hand, the whole CB is mainly dominated equally by the S and Sb atoms, with negligible contribution of Ag atoms. Further examination of the partial density of states (PDOS), in Figure 10(b), shows that the lower states of the VB are dominated by 4-*d* orbitals of Ag whereas in the top of the VB, the major contributors are the 3-*p* state of S and very minimal contributions from the 3-*p* state of Sb. The upper CB is predominantly consisting of a 3-*p* state of S (from 0.5 eV to 2.5 eV) whereas the lower regions have almost equivalent contributions by 3-*p* orbitals of both S and Sb (from 2.5 eV to 4 eV) and very negligible contribution from *s* state of Sb.

4.1.5 ZT enhancement through doping

One main strategy to enhance the ZT values of material is by optimising the carrier concentration it directly depends on the Seebeck coefficient through the Mott relations and hence directly influences the thermoelectric efficiency. In this work, we have

studied the Transport properties as function carrier concentrations ranging from 5×10^{18} - $5 \times 10^{20} \text{ cm}^{-3}$.

4.1.6 Transport properties

The transport properties were investigated with the help of AMSET. The carrier relaxation time and overall mobilities were found by considering different scattering phenomena. We studied these with varying carrier conc. at 300 K for both p- and n-type AgSbS₂ monolayers. The three main scattering phenomena included ADP, POP, and IMP; hence, the average scattering time can be found by Matthiessen's rule, which is already taken into consideration while calculating the transport properties in AMSET. The calculated scattering rates ($1/\tau$) are shown for both p- and n-type in Figure 11.

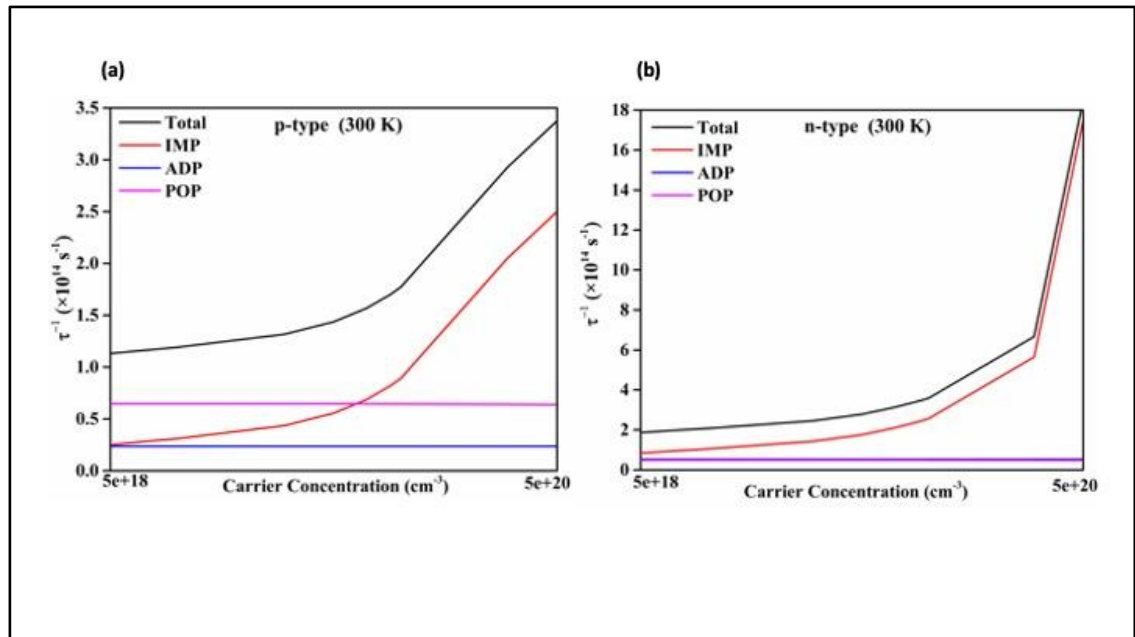


Figure 11: Scattering rates due to different scatterings in variation with carrier concentration of AgSbS₂ for (a) p-type at 300 K (b) n-type at 300 K

It can be observed from Figure 11 that both ADP and POP scattering rates exhibit no dependency on the chosen carrier concentrations. Conversely, IMP scattering rates

progressively rise with increasing carrier conc., ultimately driving the overall trend in the net scattering rate for both n- and p-type at 300 K. Altogether, the electrons contribute to higher scattering rates than the hole for the investigated AgSbS₂ monolayer. To further understand the transport properties, we examined how the mobility contributions from ADP, POP, and IMP scatterings vary with carrier concentrations at room temperature using the relation $\mu = e\tau/m^*$, where m^* is the effective mass, and e is the electronic charge. The μ of charge carriers is a direct result of the dispersion of bands, as depicted in Figure 12 at 300 K. In the case of n-type materials, we observed that as carrier concentrations increased, the μ showed a noticeable increase in the contribution from POP scattering. However, for IMP and ADP, μ exhibited a decreasing trend and eventually stabilised, reaching a nearly constant value, resulting in the overall trend driven by the μ contributions of POP. On the other hand, for the p-type at μ contributions for ADP, POP and IMP all attain a saturated state with each of them almost having constant values, driving the entire trend to be almost independent of carrier concentrations.

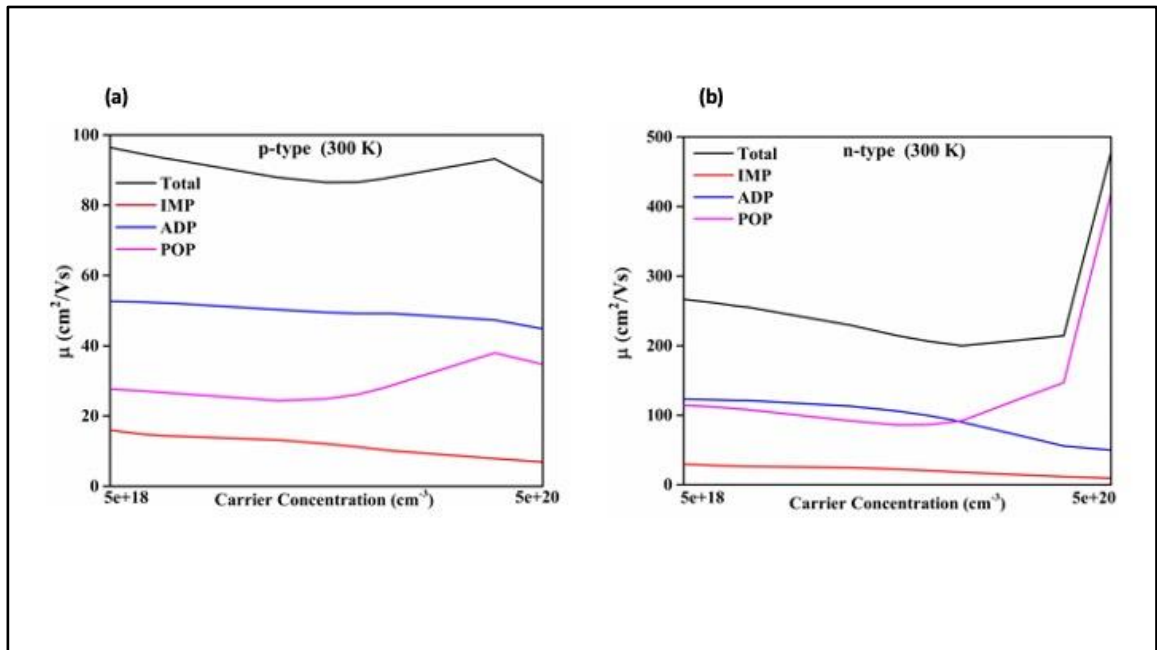


Figure 12: The Carrier Mobility of AgSbS₂ due to different scatterings in variation with carrier concentration for (a) p-type at 300 K and (b) n-type at 300 K

Next, we found S , σ , κ_e , and $S^2\sigma$ with varying carrier concentrations for both the crystallographic directions a - and b - of the AgSbS₂ monolayer at room temperature. Our findings align with the anticipated trend: the S decreases as carrier concentrations increase, consistent with the Mott equation [62]. In the case of n-type material, we observed that the S is higher in the b -direction compared to the a -direction at 300 K, as shown in Figure 13(a). In p-type material we have very minimal difference in the value variation of S along both the direction with carrier concentration. The highest value for the S for p-type is 361.62 μVK^{-1} in the a -direction and 370.72 μVK^{-1} in the b -direction, whereas for n-type was 327.47 μVK^{-1} in the a -direction and 352.82 μVK^{-1} for 300 K. these values are comparable to various state-of-the-art TE monolayers like WS₂ (328.15 μVK^{-1}) and PtTe₂ (400.15 μVK^{-1}) at 300 K [63,64].

The value of σ in the n-type material depicts a notable increase with the increase in the carrier concentration along the b -direction compared to the a -direction attaining an optimal value of 274.65×10^4 S/m in the b -direction at 300 K due to dispersive bands in the conduction region and high-value of μ for the charge carriers, Whereas in the a -direction the values are significantly low compared to b -direction hence making it independent of direction figure 13(b) Conversely, the p-type material exhibits a similar trend, it also displays a substantial increase in the b -direction compared to the a -direction attaining values up to 136.95×10^4 S/m but unlike n-type the gap between the values along both directions is significantly less hence making it direction dependent.

The value of κ_e increases significantly with the enhancement in carrier concentrations in the b -direction for the n-type, as shown in Figure 13(c) This same trend is supported by the p-type (Fig. 6c). The divergent patterns observed in σ and S yield high $S^2\sigma$ values for n-type materials in the b -direction at 300 K attaining high values of 10.66 $\text{mWm}^{-1}\text{K}^{-2}$ and 11.13 $\text{mWm}^{-1}\text{K}^{-2}$ which is significantly higher than in the a -direction, in p-type materials, a similar trend is observed in both directions but the values are lower compared to the n-type shown in Figure 13(d). Due to the weak bonding characteristics and high atomic mass of AgSbS₂ we have an appreciably low value of Debye temperature according to Slack's theory hence the Lattice thermal conductivity can't

be found out using Slack's model as it holds for higher values of Debye temperature and hence we calculated using the Cahill model, given by the following expression[65]:

$$\kappa_l = k_B p^{2/3} (v_l + 2v_t) / 2.48 \quad (25)$$

Here, K_B stands for the Boltzmann constant, p is the total number of atoms per unit volume, v_l and v_t are longitudinal and transverse sound velocities, respectively at room temperature. we found the normalised κ_l of $0.205 \text{ Wm}^{-1}\text{k}^{-1}$ along the a -direction and $0.306 \text{ Wm}^{-1}\text{k}^{-1}$.

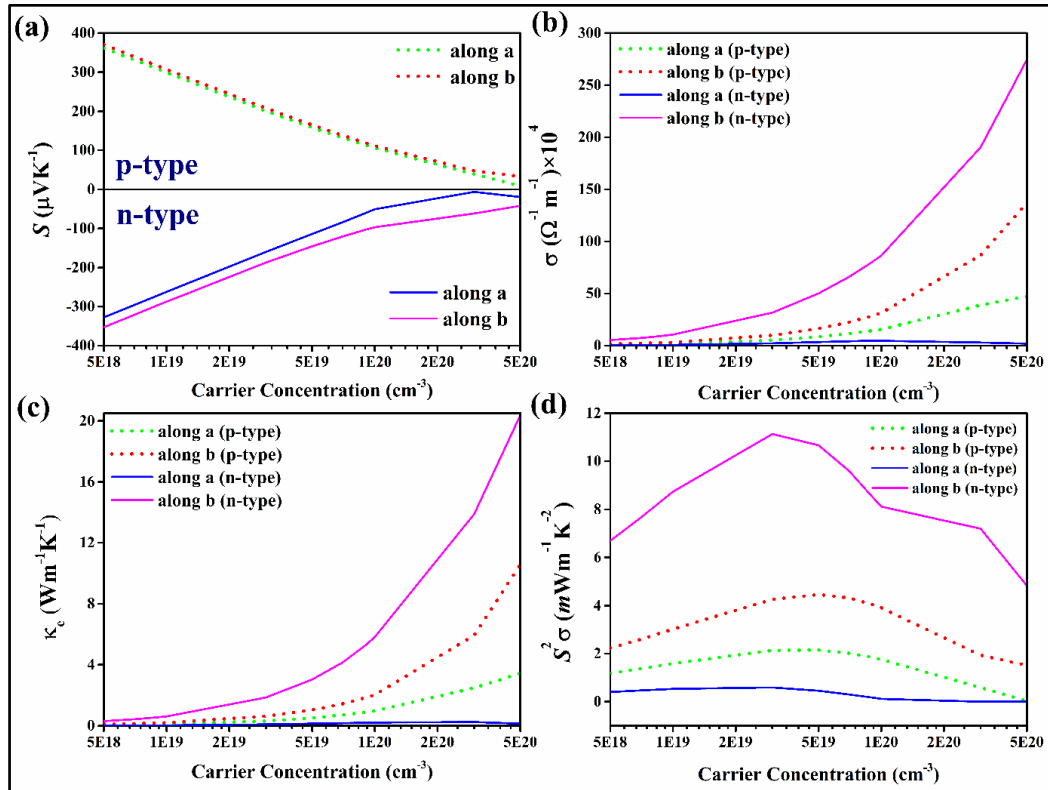


Figure 13: (a)The Seeback coefficient (b) the electrical conductivity (c) the electronic contribution for thermal conductivity (d) the power factor for both p- and n-type AgSbS₂ along *a*-and *b*-direction at 300 K

4.1.7 Thermoelectric Figure of Merit

The ZT values are found in a - and b - directions at 300 K as a function of carrier conc. expressed as $ZT=S^2\sigma T/\kappa$ for both n and p-type. As the carrier concentration increases, the ZT value decreases from its peak values to attain lower values in both directions at 300 K, as shown in Figure 14. ZT values are obtained for both n- and p-type at a carrier concentration of $5\times 10^{18} - 5\times 10^{20}\text{cm}^{-3}$, having values going up to 0.3 and 0.2 in both a - and b - directions, respectively for p-type at 300 K. Whereas for n-type, the values go as high as 0.5 in b - direction at 300 K for a doping concentration of 1×10^{19} . n-type materials express higher ZT values than p-type materials in both directions. On closer examination, we observed particularly elevated ZT values in the b -direction. As the doping goes up to the order 10^{20}cm^{-3} , the ZT reduced to very low values in both directions at 300 K. These ZT values are undoubtedly comparative to various TEs like $\text{RBZn}_4\text{P}_3(0.33)$, $\text{MoS}_2(0.6)$ and $\text{Mg}_3\text{Sb}_2(0.6)$ at room temperature[66,67] . There is a further potential for increasing the thermoelectric efficiency of the material through strain engineering application which we intend to study in our further works.

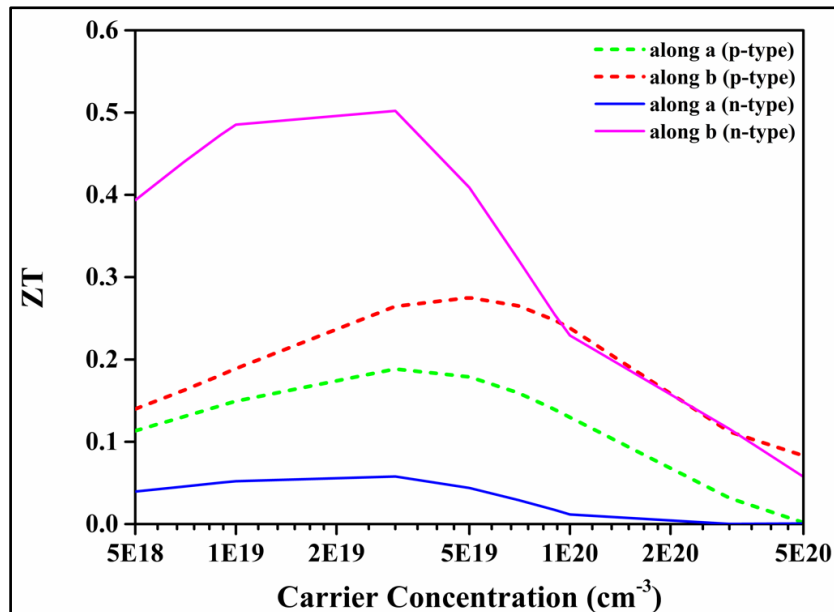


Figure 14: The TE Figure of Merit at 300 K in the a - and b direction in variation with carrier concentration for n- and p-type

4.2 Results and Discussion for KCd_4P_3

4.2.1 Structural properties

The ternary KCd_4P_3 phase is formed in the centrosymmetric rhombohedral space group $R\bar{3}m$ (No. 166) shown in Figure 15. The asymmetric unit has five crystallographic unique atoms K, Cd1, Cd2, P1 and P2. There are 24 atoms in the unit cell occupying the Wykoff positions 3b, 6c, 6c, 6c and 3b. $[\text{Cd}_4\text{P}_3]^-$ polyanions comprised of condensed CdP_4 tetrahedra. The layers of this structure are stacked along the c - direction of the crystal structure in an ABCABC sequence, with layers of K^+ cations in between. The structure of polyanions is mainly comprised of two independent Cd and two independent atoms of P. atoms are coordinated tetrahedrally with P-Cd-P angles very close to 104° and the corresponding Cd-P bond length is 2.79 Å, as presented in Table 3. The optimized lattice parameters of KCd_4P_3 were found and matched with its experimental results

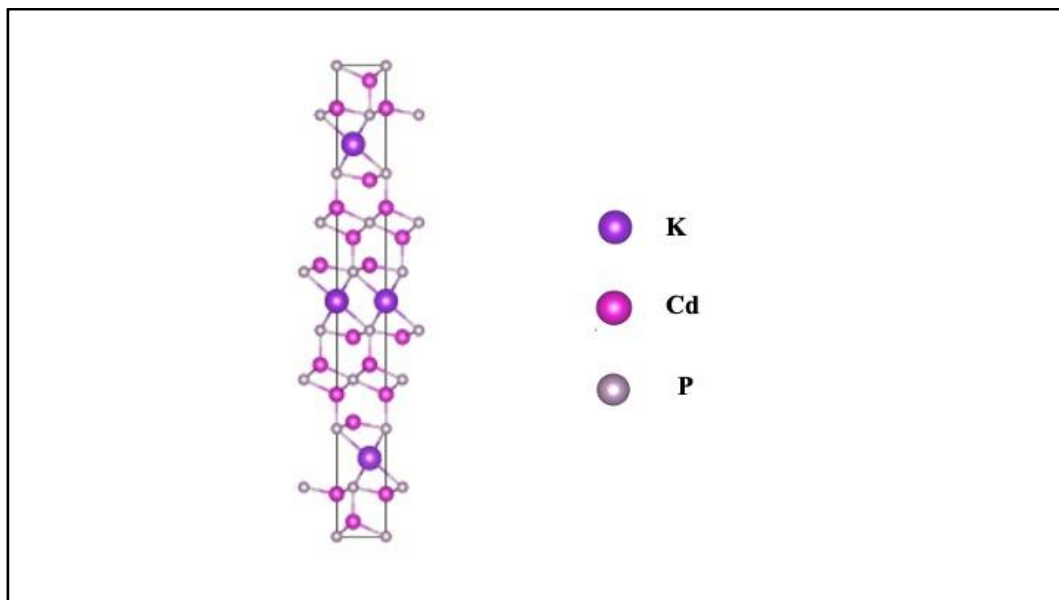


Figure 15: The side view of the KCd_4P_3 bulk structure

Table 3. Obtained lattice constants (a and c in Å), volume (V in Å³) and bond lengths (in Å) of KCd₄P₃ in comparison with its experimental results.

Material KCd ₄ P ₃	Structural parameters			Bond length (Å)
	a=b(Å)	c (Å)	V (Å ³)	Cd1-P1 / K1-P1
Present work	4.42	35.76	605.27	2.58/3.38
Experimental[68]	4.34	33.19	542.60	2.56/3.34

4.4.2 Computational details

The electronic structure and structural calculations of KCd₄P₃ were performed using the full potential LAPW as implemented in WIEN2k. The PBE-GGA was utilized for structural optimization where the KSE were solved self consistently till meeting the convergence criterion. The electronic structure calculations were performed using the TB-mBJ approach to estimate the accurate band gap as GGA underestimates the band gap. The cuff-off parameter $R_{mt}K_{max}$ was set to be 7. For the self-consistent calculation 3000 k -points having 30x30x3 k- mesh were used with an energy convergence of 0.0001 Ry. The TE properties were found by solving the BTE with CRTA and RBA which is incorporated in the BoltzTraP code.

4.2.3 Electronic structure

The band structure and the DOS are essential parameters that give us information about the electronic and transport properties. The band structure was calculated using the TB-mBJ approach as shown in Figure 16(a). KCd₄P₃ shows a direct band gap of 0.66 eV at 0% strain

With both VBM and CBM at the Γ point this remains consistent even after the impact of strain. The analysis of the density of states (DOS) shown in Figure 16(b) the major

contributions in the valence band by P, Cd and very minimal contribution by potassium(K) from -3 eV to 0 eV and upon analyzing the projected density of states (PDOS) depicted in Figure 16(c) from -3 eV to 0 eV we see the major contribution by P-*p* followed by Cd-*p* states suggesting that the transport properties of the compound are primarily governed by the polyanionic substructure and below -3 to -5 eV we see dominant contributions from P-*p* and Cd-*s*. lower energies are found to be with the Cd-*d* and the P 3-*s* lone pairs. Now when we go above the Fermi level, we see evident contributions from Cd and P., upon further analysis of PDOS we see major contributions of P-*p*, Cd-*s* and Cd-*p* states dominating the CB. The CBM and the VBM band are both determined by the hybridized orbitals of P and Cd, indicating a substantial presence of covalent Cd-P bonds. As a result, covalent bonds exist within the network, interacting with positive electrical metal cations through ionic bonding. Ionic and covalent bonds can be seen to coexist in different Zintl phase compounds [69]. The strain effect on the electronic structure of the KCD_4P_3 was investigated where the biaxial strain that is in-plane is defined as $\varepsilon = (a - a_0)/a_0$ in the *a*-direction and $\varepsilon = (c - c_0)/c_0$ similarly in the *c*-direction where *a* and *a*₀ represent the strained and unstrained structure's corresponding lattice constants. The band structure of the strained structure can be seen in Figure 17. Tensile and compressive strains of 2% and 4% strain were applied in both the *a* and *c*-directions and the variation was studied. we can see with the increase of the compressive strain the E_g value decreases from 0.66 eV to 0.54 eV whereas the E_g value increases with an increase in tensile strain from 0.66 eV to 0.76 eV. These band gap value changes show how fluctuations in strains dynamically change the band structure leading to an impact on the transport properties [70].

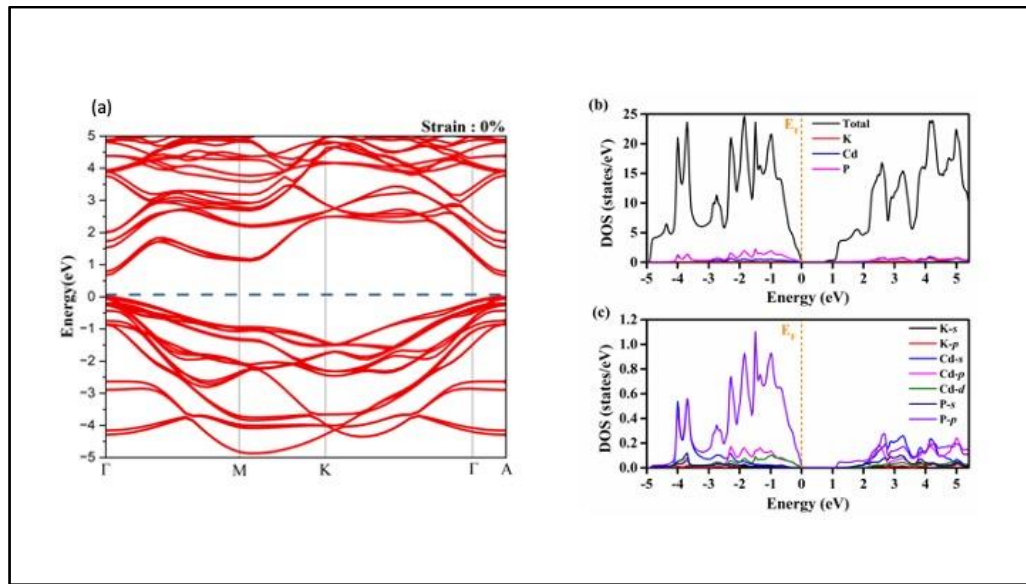


Figure 16(a) Electronic band structure (b)DOS of KCD₄P₃ (c) PDOS of KCD₄P₃

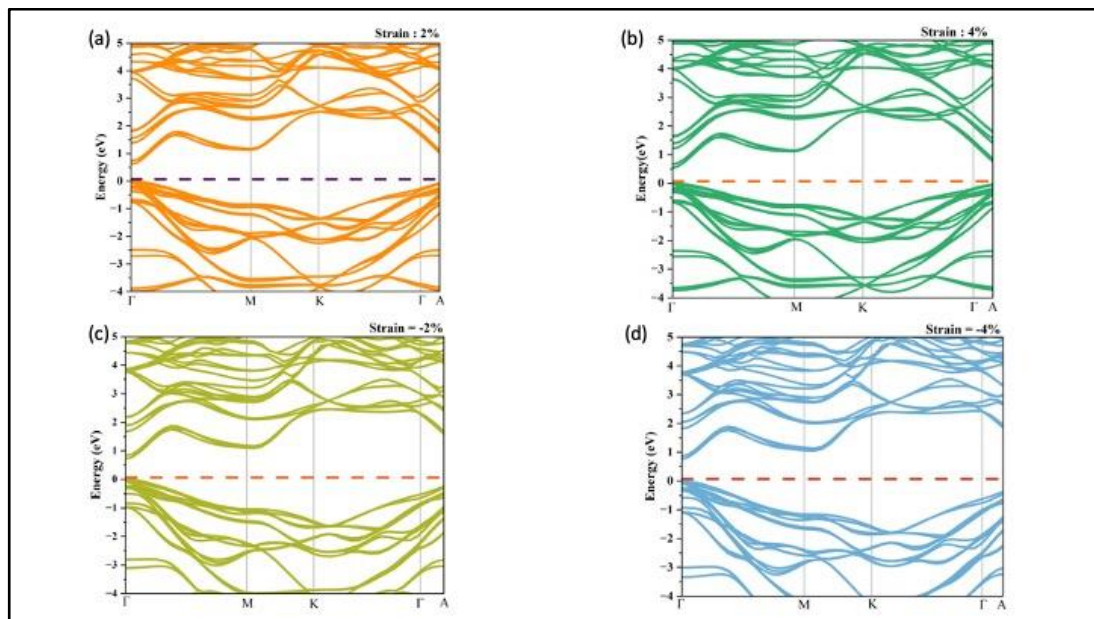


Figure 17: Electronic band structure of KCD₄P₃ with (a) 2% strain (b) 4% strain (c) -2% strain (d) -4% strain

4.2.4 ZT enhancement through strain engineering

The effect of strain has been shown to tune the electronic and hence transport properties of materials. For example, S in phosphorene can be enhanced greatly by strain-induced band convergence leading to a high ZT value of 2.12 for an applied strain of 8% at room temperature. κ can be also increased or decreased by applied strains, depending on material characteristics.

Mg₃Sb₂ has shown remarkable growth in its TE performance by the application of biaxial strain that enabled the tuning of band structure so that the band degeneracy of the valence and conduction band increases, leading to an increase in the value of S and power factor, hence, producing a ZT value of 2.6 around -2.5% strain at room temperature.

4.2.5 Transport properties

The TE parameters of KCd₄P₃ were found by solving BTE through the BoltzTraP code along with the CRTA, which means S does not depend on the scattering rate (τ), so presuming that temperature and doping levels do not affect the electrical band structure.[71] The TE properties are found as a function of temperature. We see in the a -direction with an increase in temperature S/τ decreases from its peak value of 249 μ V/K at 350K for a tensile strain of 2% and increases with tensile strain and decreases with compressive strains in a -direction whereas on the contrary in the c -direction we see an increase of S/τ with temperature and compressive strain reaching a value of 260 μ V/K at 4% compressive strain as shown in Figure 18. The Seebeck coefficient has a decreasing trend in both directions but it rapidly changes its course after a certain temperature for each particular strain and starts rising in the c -directions but in the a -direction it steadily decreases with temperature. The non negative value of S denotes the majority of charge carriers as holes, making it a p -type semiconductor [72]. The decrease of the S compensates for the increase of σ and thus the maximal $S^2\sigma$ of KCD₄P₃ in both directions with lower band gap values.

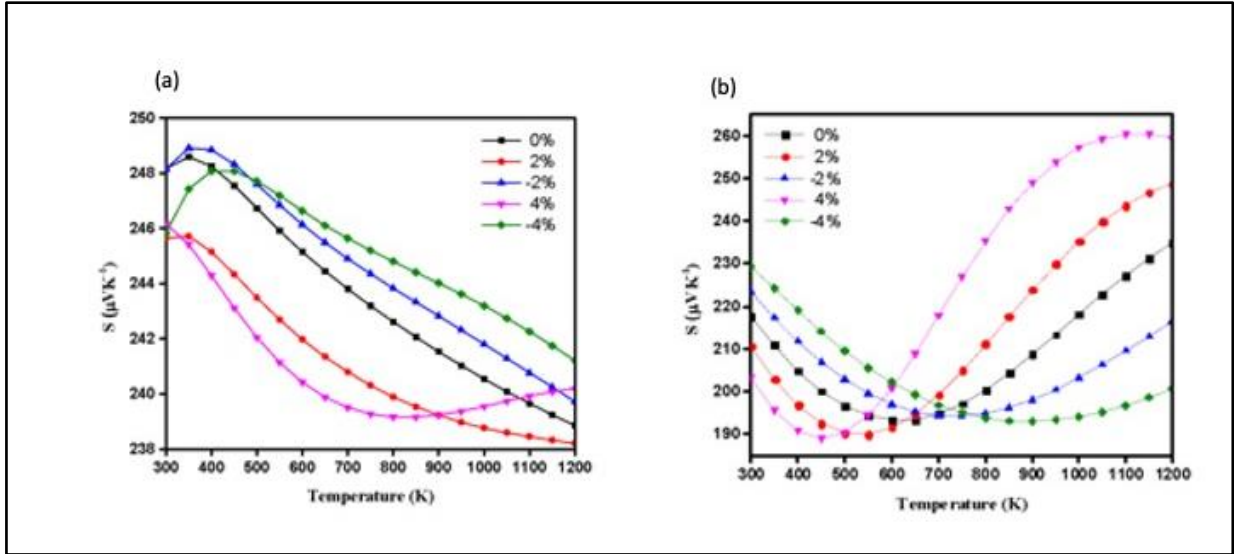


Figure 18: S/τ of KCD_4P_3 (a) in the a -direction (b) in the c -direction

σ/τ increases for both a - and c - directions with the increase in compressive and tensile strain but it attains comparatively higher values with compressive strain in the a -direction whereas in the c -direction higher values are attained by the tensile strain attaining a value of $11 \times 10^{18} \Omega^{-1}\text{m}^{-1}\text{s}^{-1}$ and $0.7 \times 10^{18} \Omega^{-1}\text{m}^{-1}\text{s}^{-1}$ respectively as shown in Figure 19. We see the trend of S and σ/τ are showing opposite trends with an increase of temperature and strain hence the determination of whether the applied strain will enhance or hinder the electronic transport properties depends on the interplay between two competing factors.

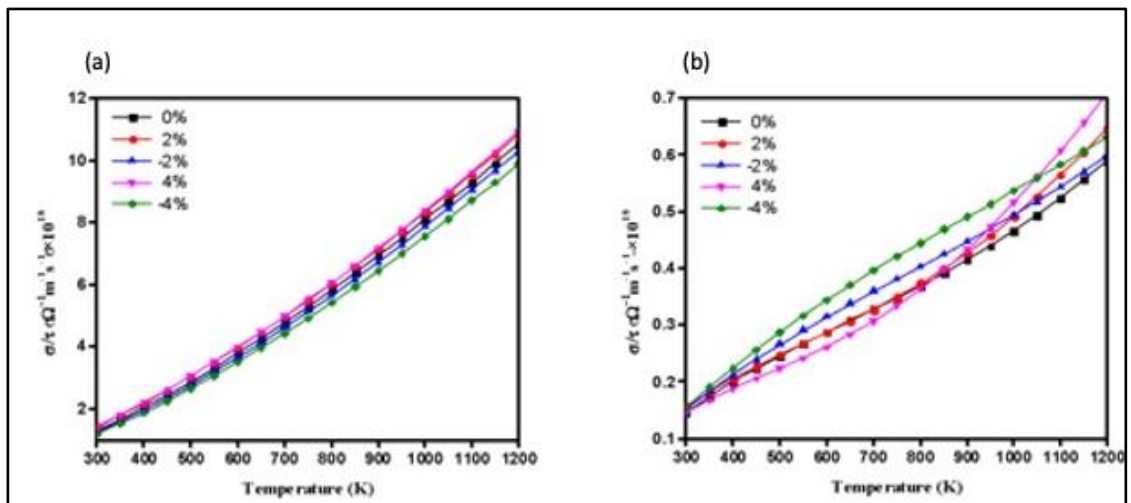


Figure 19: σ/τ of KCD_4P_3 (a) in the a -direction (b) in the c -direction

κ_e/τ increases with temperature in both directions, In the a -directions we see no significant difference in the value of κ_e/τ with both tensile and compressive strain, the system attains a maximum value of $11 \times 10^{14} \text{ Wm}^{-1}\text{K}^{-1}\text{s}^{-1}$ around 1200K as shown in Figure 20. It shows similar behaviour as σ/τ , as κ_e and σ is interrelated by Wiedemann Franz law, $\kappa_e = L\sigma T$ but highly dependent on temperature. The actual values of the transport coefficients were calculated by incorporating the approximated relaxation time of $\tau=10^{14}$ sec. In the c -direction, we can see κ_e/τ increases significantly with increased temperature and compressive strains reaching a maximum value of $0.7 \times 10^{14} \text{ Wm}^{-1}\text{K}^{-1}\text{s}^{-1}$ at 1200 K. We don't see any significant impact of strain at room temperature.

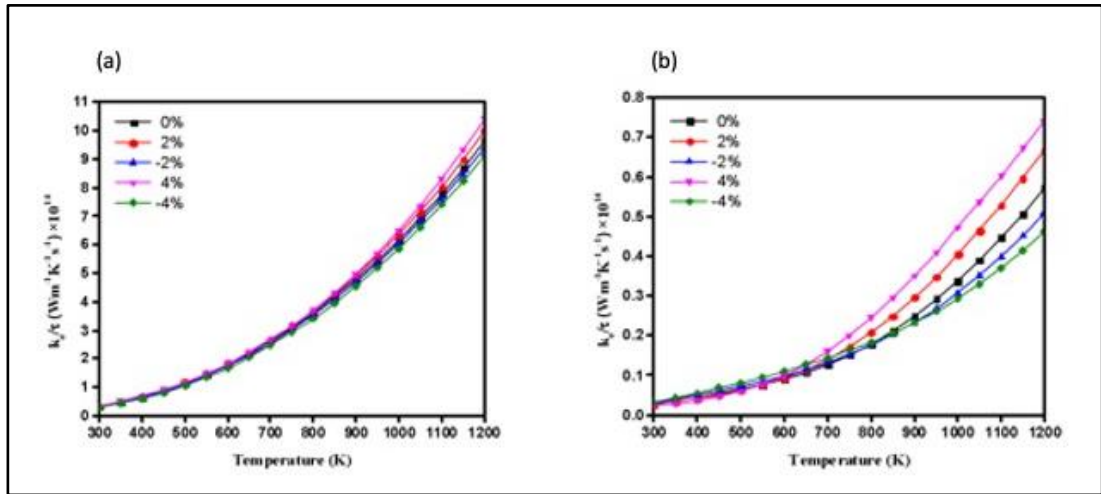


Figure 20: κ_e/τ of KCD_4P_3 (a) in the a -direction (b) in the c -direction

The power factor decides the actual trend of the figure of merit, $S^2\sigma$ compensates for the contrasting trends of both S and σ . The decrement of S with the increase in tensile strain or compressive strain is compensated by an increment σ leading to an optimal value of the power factor. $S^2\sigma$ has a very little significant impact on strain in the a -

direction, the value rises to a value of $6.4 \times 10^{11} \text{ Wm}^{-1}\text{k}^{-2}\text{s}^{-1}$. On the contrary in the c -direction, $S^2\sigma$ increases with compressive strain reaching an optimal value of $0.45 \times 10^{11} \text{ Wm}^{-1}\text{k}^{-2}\text{s}^{-1}$ around 1200 K at 4%, the trend remains almost similar to what was in the a -direction but only up to 700 K after that with temperature we see the impact of strains on the power factor values. Figure 21(b) shows that the compressive strain is significantly higher than its unstrained component. Hence the significant rise in the power factor guarantees a higher and enhanced figure of merit.

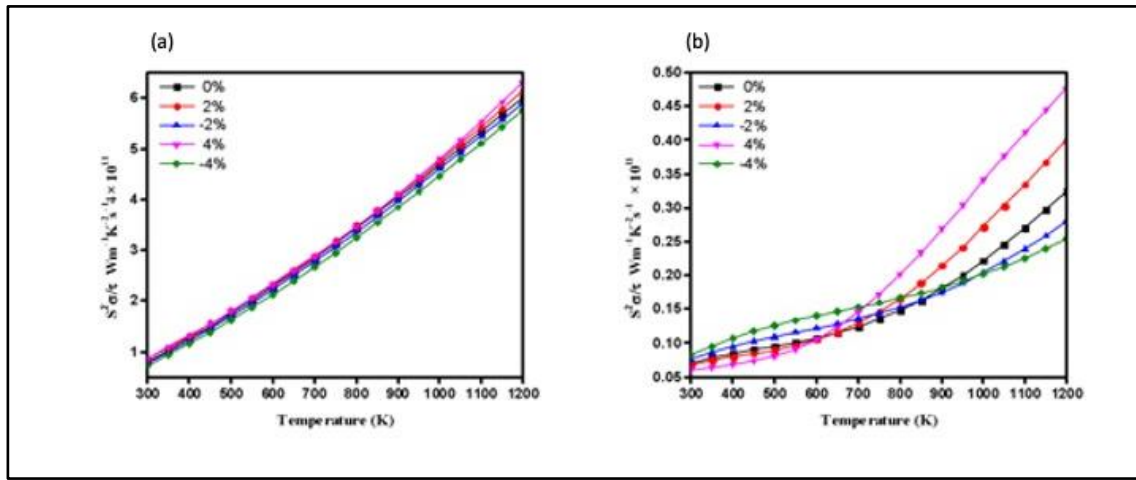


Figure 21: $S^2\sigma$ of KCD_4P_3 (a) in the a -direction (b) in the c -direction

4.2.6 Thermoelectric figure of merit

The ZT values are found in both the a - and c - directions for KCD_4P_3 as a function of temperature ranging from 300 K and 1200K as shown in Figure 22, for this study, we have ignored the contribution of the lattice thermal conductivity and only considered the maximum value of ZT . We see that the value of ZT increases initially and then decreases strain increment and temperature. We see in the a -direction that the optimal ZT value is contributed by both compressive and tensile strains attaining a value of as high as 0.76 at room temperature but then the contribution of the compressive strain to ZT is drastically decreased with an increase in temperature compared to the tensile strain contributions. In the c -direction, the ZT value decreases with temperature up to a point and then reverts back to the increasing trend. The optimal ZT value is achieved

at a room temperature of 0.77, in this case, the contribution of compressive strain follows the same trend as in the a -direction but up to a certain limit of around 650 K and then we see a rapid rise in the contributions of the compressive strain at the other hand the tensile strain gets saturated attaining back the optimal value of 0.77 at 1200K. The values of ZT of our system are higher at room temperature with its iso-structure RbZn_4P_3 which has a reported value of 0.33 at 300K whereas KCD_4P_3 reports a value of 0.77 at room temperature in the c -direction for a compressive strain of 4%. This shows KCD_4P_3 to be a good potential thermoelectric device and can be a good candidate for future thermoelectric applications.

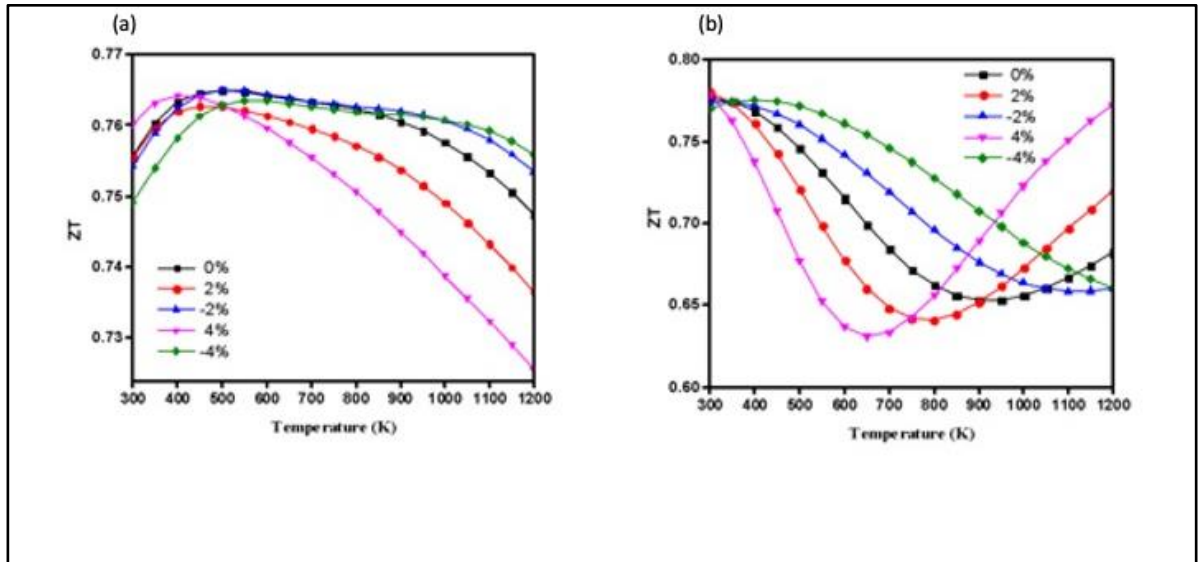


Figure 22: ZT of KCD_4P_3 (a) in the a -direction (b) in the c -direction

CONCLUSION AND FUTURE SCOPE

In this study, we have used first-principles calculations in conjunction with semiclassical Boltzmann transport theory to realize the high ZT of AgSbS_2 monolayer at 300 K along a - and b - crystallographic directions. We have analysed the effect of carrier concentration on its TE performance. AgSbS_2 is thermodynamically and mechanically stable, confirmed by its cohesive energy and elastic constants. The elastic properties have confirmed its covalent bonding in the a -direction; it has also been found that AgSbS_2 is anisotropic and ductile. The electronic band structure has shown that AgSbS_2 is an indirect semiconductor, having an indirect band gap of around 1.31 eV using hybrid functional. The calculated unit cell parameters and various bond lengths have been found comparable with a previous similar study on CuSbS_2 monolayer. The n-type AgSbS_2 monolayer at an optimized carrier concentration of $5 \times 10^{18} \text{ cm}^{-3}$ exhibited peak ZT values of 0.5 in the b -directions at 300 K. These promising ZT values make AgSbS_2 an optimal thermoelectric material for the future. Our findings on the electronic and transport properties of the AgSbS_2 monolayer may open new horizons for the design and synthesis of more efficient silver-based chalcogenides thermoelectric.

For the second work, we followed the same theory as the first work to analyze the ZT of KCD_4P_3 at different temperature ranges in both a - and c -directions of the crystal structure. The structure meets all the stability criteria as it was found to be experimentally synthesized, hence the structure is thermodynamically, elastically and dynamically stable. The electronic band structure calculations show KCD_4P_3 to be a direct band gap semiconductor with an E_g of 0.66 eV using the TB-mBJ approach. The calculated lattice parameters and bond-length values match the experimental values. To enhance the ZT values we applied biaxial tensile and compressive strains in both a - and c -directions and saw the changes in the transport properties with the increment in strain in both directions. We saw a significant rise in the ZT values at higher

temperatures in the c -directions with the increase in compressive strain reaching a value of approximately 0.77 at 1200 K and in the a -direction, there is a decline in the ZT value at high temperatures with increasing compressive and tensile strain attaining a value of 0.76 at room temperature in the a -direction. These promising ZT values make KCD_4P_3 an optimal thermoelectric material for the future. Our findings on the electronic and transport properties of the KCD_4P_3 would open new gateways for design and synthesis of optimal Zintl phase thermoelectric materials.

REFERENCES

- [1] T. Mori, S. Priya, Materials for energy harvesting: At the forefront of a new wave, MRS Bull. 43 (2018) 176–180.
- [2] F. Zareef, M. Rashid, A.A.H. Ahmadini, T. Alshahrani, N.A. Kattan, A. Laref, Optoelectronic and thermoelectrical and mechanical properties of CdLu₂X₄ (X = S, Se) using first-principles calculations for energy harvesting applications, Mater. Sci. Semicond. Process. 127 (2021) 105695. <https://doi.org/10.1016/j.mssp.2021.105695>.
- [3] M. Roknuzzaman, K. Ostrikov, H. Wang, A. Du, T. Tesfamichael, Towards lead-free perovskite photovoltaics and optoelectronics by ab-initio simulations, Sci. Rep. 7 (2017) 14025. <https://doi.org/10.1038/s41598-017-13172-y>.
- [4] G. Tan, M. Ohta, M.G. Kanatzidis, Thermoelectric power generation: from new materials to devices, Philos. Trans. R. Soc. Math. Phys. Eng. Sci. 377 (2019) 20180450. <https://doi.org/10.1098/rsta.2018.0450>.
- [5] L.E. Bell, Cooling, Heating, Generating Power, and Recovering Waste Heat with Thermoelectric Systems, Science 321 (2008) 1457–1461. <https://doi.org/10.1126/science.1158899>.
- [6] Christophe Goupil, Henni Ouerdane, Knud Zabrocki, Wolfgang Seifert, Nicki F. Hinsche, Eckhard Müller, ‘Thermodynamics and thermoelectricity’, 2016, Goupil, Christophe (ed.). Continuum Theory and Modeling of Thermoelectric Elements. New York: Wiley-VCH. pp. 2–3. ISBN 9783527413379.
- [7] Seebeck, ‘Magnetische Polarisation der Metalle und Erze durch Temperatur-Differenz’ [Magnetic polarization of metals and ores by temperature differences],

1882, Abhandlungen der Königlichen Akademie der Wissenschaften zu Berlin (in German).

[8] ‘Thermoelectric effect’, Wikipedia.

[9] O.L. Anderson, A simplified method for calculating the debye temperature from elastic constants, *Journal of Physics and Chemistry of Solids*. 24 (1963) 909–917. [https://doi.org/10.1016/0022-3697\(63\)90067-2](https://doi.org/10.1016/0022-3697(63)90067-2).

[10] V. Tayari, B.V. Senkovskiy, D. Rybkovskiy, N. Ehlen, A. Fedorov, C.-Y. Chen, J. Avila, M. Asensio, A. Perucchi, P. Di Pietro, L. Yashina, I. Fakih, N. Hemsworth, M. Petrescu, G. Gervais, A. Grüneis, T. Szkopek, Quasi-two-dimensional thermoelectricity in SnSe, *Phys. Rev. B*. 97 (2018) 045424. <https://doi.org/10.1103/PhysRevB.97.045424>.

[11] S. Huang, Z. Wang, R. Xiong, H. Yu, J. Shi, Significant enhancement in thermoelectric performance of Mg₃Sb₂ from bulk to two-dimensional monolayer, *Nano Energy*. 62 (2019) 212–219. <https://doi.org/10.1016/j.nanoen.2019.05.028>.

[12] Y. Xiao, L.-D. Zhao, Charge and phonon transport in PbTe-based thermoelectric materials, *Npj Quant Mater*. 3 (2018) 55. <https://doi.org/10.1038/s41535-018-0127-y>.

[13] Li, D., Gong, Y., Chen, Y. et al. Recent Progress of Two-Dimensional Thermoelectric Materials. *Nano-Micro Lett*. 12, 36 (2020).

[14] Tran, VT., Saint-Martin, J., Dollfus, P. et al. Optimizing the thermoelectric performance of graphene nano-ribbons without degrading the electronic properties. *Sci Rep* 7, 2313 (2017).

[15] H. Y. Lv, W. J. Lu, D. F. Shao, and Y. P. Sun, “Enhanced thermoelectric performance of phosphorene by strain-induced band convergence,” *Phys. Rev. B*, vol. 90, no. 8, p. 085433, Aug. 2014, doi: 10.1103/PhysRevB.90.085433.

- [16] Gangjian Tan, Li-Dong Zhao, and Mercuri G. Kanatzidis *Chemical Reviews* 2016 116 (19), 12123-12149 DOI: 10.1021/acs.chemrev.6b00255.
- [17] C. Chen et al., “Intrinsic nanostructure induced ultralow thermal conductivity yields enhanced thermoelectric performance in Zintl phase Eu_2ZnSb_2 ,” *Nat. Commun.*, vol. 12, no. 1, p. 5718, Sep. 2021, doi: 10.1038/s41467-021-25483-w.
- [18] S. M. Kauzlarich, S. R. Brown, and G. Jeffrey Snyder, “Zintl phases for thermoelectric devices,” *Dalton Trans.*, no. 21, p. 2099, 2007, doi: 10.1039/b702266b.
- [19] S. Berri, “First-principles Study on Half-metallic Properties of the CoMnCrSb Quaternary Heusler Compound,” *Journal of Superconductivity and Novel Magnetism*, vol. 29, no. 5, pp. 1309–1315, May 2016, doi: 10.1007/s10948-016-3404-7.
- [20] L. Bainsla and K. G. Suresh, “Equiatomic quaternary Heusler alloys: A material perspective for spintronic applications,” *Applied Physics Reviews*, vol. 3, no. 3. American Institute of Physics Inc., Sep. 01, 2016. doi: 10.1063/1.4959093.
- [21] A. Planes, L. Mãosa, and M. Acet, “Magnetocaloric effect and its relation to shape-memory properties in ferromagnetic Heusler alloys,” *Journal of Physics Condensed Matter*, vol. 21, no. 23, 2009, doi: 10.1088/0953-8984/21/23/233201.
- [22] K. Özdoğan, E. Şaşıoğlu, and I. Galanakis, “Slater-Pauling behavior in LiMgPdSn -type multifunctional quaternary Heusler materials: Half-metallicity, spin-gapless and magnetic semiconductors,” *Journal of Applied Physics*, vol. 113, no. 19, May 2013, doi: 10.1063/1.4805063.
- [23] Zheng, ZH., Shi, XL., Ao, DW. et al. Harvesting waste heat with flexible Bi_2Te_3 thermoelectric thin film. *Nat Sustain* 6, 180–191 (2023). <https://doi.org/10.1038/s41893-022-01003-6>

- [24] R Carlini, C F Fanciulli, P. Boulet, M C Record, V V Romaka, et al.. Skutterudites for Thermoelectric Applications: Properties, Synthesis and Modelling. Cristina Artini. Alloys and Intermetallic Compounds: From Modeling to Engineering, CRC press Taylor&Francis, 2017, 9781498741439. fhal01483329f.
- [25] Xi Zhang, Yuqiao Zhang, Liao Wu, Akihiro Tsuruta, Masashi Mikami, Hai Jun Cho, and Hiromichi OhtaACS Applied Materials & Interfaces 2022 14 (29), 33355-33360DOI: 10.1021/acsami.2c08555.
- [26] ‘Density functional theory’, Wikipedia
- [27]<https://www.cambridge.org/core/books/electronicstructure/DDFE838DED61D7A402FDF20D735BC63A>
- [28]https://www.vasp.at/wiki/index.php/Category:Exchange-correlation_functionals
- [29] Harald Ibach, Hans Lüth, ‘Solid-State Physics’, Springer
- [30] <https://www.vasp.at/info/about/>
- [31] Georg K.H. Madsen, Jesús Carrete, Matthieu J. Verstraete, ‘BoltZTraP2, a program for interpolating band structures and calculating semi-classical transport coefficients’, 2018, Elsevier, Computer Physics Communications.
- [32] <https://hackingmaterials.lbl.gov/amset/>
- [33] Ouyang, Y. & Guo, J. A theoretical study on thermoelectric properties of graphene nanoribbons. Appl. Phys. Lett. 94, 263107, (2009)
- [34] Mazzamuto, F. et al. Enhanced thermoelectric properties in graphene nanoribbons by resonant tunnelling of electrons. Phys. Rev. B 83, 235426, (2011).
- [35] Naguib, M., Mochalin, V.N., Barsoum, M.W. and Gogotsi, Y. (2014), 25th Anniversary Article: MXenes: A New Family of Two-Dimensional Materials. Adv. Mater., 26: 992-1005.
- [36] Xu, T., Wang, Y., Xiong, Z. et al. A Rising 2D Star: Novel MBenes with Excellent Performance in Energy Conversion and Storage. Nano-Micro Lett. 15, 6 (2023).
- [37] Peijie Liu, Mengnan Wu, Ghulam Abbas, Weifan Yang, Fusheng Liu, Yu Li, Transport behaviour and thermoelectric properties of SnSe/SnS heterostructure

modulated with asymmetric strain engineering, *Computational Materials Science*, Volume 207, 2022, 111271, ISSN 0927-0256

[38] Jisook Hong, Changhoon Lee, Jin-Seong Park, and Ji Hoon Shim, *Phys. Rev. B* 93, 035445 (2016)

[39] K. Hoang, S.D. Mahanti, J.R. Salvador, M.G. Kanatzidis, Atomic Ordering and Gap Formation in Ag-Sb-Based Ternary Chalcogenides, *Phys. Rev. Lett.* 99 (2007) 156403. <https://doi.org/10.1103/PhysRevLett.99.156403>.

[40] S.Y. Tee, D. Ponsford, C.L. Lay, X. Wang, X. Wang, D.C.J. Neo, T. Wu, W. Thitsartarn, J.C.C. Yeo, G. Guan, T. Lee, M. Han, Thermoelectric Silver-Based Chalcogenides, *Advanced Science*. 9 (2022) 2204624. <https://doi.org/10.1002/advs.202204624>.

[41] M. Jin, J. Liang, P. Qiu, H. Huang, Z. Yue, L. Zhou, R. Li, L. Chen, X. Shi, Investigation on Low-Temperature Thermoelectric Properties of Ag₂Se Polycrystal Fabricated by Using Zone-Melting Method, *J. Phys. Chem. Lett.* 12 (2021) 8246–8255. <https://doi.org/10.1021/acs.jpcclett.1c02139>

[42] S. Lin, W. Li, X. Zhang, J. Li, Z. Chen, Y. Pei, Sb induces both doping and precipitation for improving the thermoelectric performance of elemental Te, *Inorg. Chem. Front.* 4 (2017) 1066–1072. <https://doi.org/10.1039/C7QI00138J>.

[43] T. Chen, K. Zhang, H. Wang, W. Su, F. Mehmood, T. Wang, J. Zhai, X. Wang, T. Huo, C. Wang, The high thermoelectric performance of slightly Sb doped PbTe alloys, *J. Mater. Chem. C* 8 (2020) 1679–1685. <https://doi.org/10.1039/C9TC06124J>.

[44] W. Fang, Y. Chen, K. Kuang, M. Li, Excellent Thermoelectric Performance of 2D CuMN₂ (M = Sb, Bi; N = S, Se) at Room Temperature, *Materials* 15 (2022) 6700. <https://doi.org/10.3390/ma15196700>.

- [45] K. Lv, C. Shi, Y. Yang, Q. Wang, X. Sun, W. Chen, The pyrolysis preparation of the compact and full-coverage AgSbS₂ thin films and the photovoltaic performance of the corresponding solar cells, *J. Mater. Sci. Technol.* 98 (2022) 268–271. <https://doi.org/10.1016/j.jmst.2021.04.070>.
- [46] J. Winterlik, G. H. Fecher, A. Thomas, and C. Felser, “Superconductivity in palladium-based Heusler compounds,” *Physical Review B - Condensed Matter and Materials Physics*, vol. 79, no. 6, Feb. 2009, doi: 10.1103/PhysRevB.79.064508.
- [47] Srishti Singh, Dinesh C. Gupta. Lanthanum-based quaternary Heusler alloys LaCoCrX (X = Al, Ga): Hunt for half-metallicity and high thermoelectric efficiency. *Results in Physics*, Volume 13, June 2019, 102300.
- [48] S. M. Kauzlarich, S. R. Brown, and G. Jeffrey Snyder, “Zintl phases for thermoelectric devices,” *Dalton Trans.*, no. 21, p. 2099, 2007, doi: 10.1039/b702266b.
- [49] R. Nesper, “The Zintl-Klemm Concept – A Historical Survey,” *Z. Für Anorg. Allg. Chem.*, vol. 640, no. 14, pp. 2639–2648, Nov. 2014, doi: 10.1002/zaac.201400403.
- [50] J. Wang, B. Owens-Baird, and K. Kovnir, “From Three-Dimensional Clathrates to Two-Dimensional Zintl Phases AMSb₂ (A = Rb, Cs; M = Ga, In) Composed of Pentagonal M–Sb Rings,” *Inorg. Chem.*, vol. 61, no. 1, pp. 533–541, Jan. 2022, doi: 10.1021/acs.inorgchem.1c03217.
- [51] C. Chen et al., “Zintl-phase Eu₂ZnSb₂: A promising thermoelectric material with ultralow thermal conductivity,” *Proc. Natl. Acad. Sci.*, vol. 116, no. 8, pp. 2831–2836, Feb. 2019, doi: 10.1073/pnas.1819157116.
- [52] Unravelling the Ultralow Thermal Conductivity of Ternary Antimonide Zintl Phase RbGaSb₂: A First-principles Study,” *Indian J. Pure Appl. Phys.*, 2023, doi: 10.56042/ijpap.v61i9.3152.

[53] A. M. Medina-Gonzalez et al., “Ternary ACd₄P₃ (A = Na, K) Nanostructures via a Hydride Solution-Phase Route,” *ACS Mater. Au*, vol. 1, no. 2, pp. 130–139, Nov. 2021, doi: 10.1021/acsmaterialsau.1c00018.

[54] A. Ovchinnikov and S. Bobev, “Zintl phases with group 15 elements and the transition metals: A brief overview of pnictides with diverse and complex structures,” *J. Solid State Chem.*, vol. 270, pp. 346–359, Feb. 2019, doi: 10.1016/j.jssc.2018.11.029.

[55] J. Heyd, G.E. Scuseria, Efficient hybrid density functional calculations in solids: Assessment of the Heyd–Scuseria–Ernzerhof screened Coulomb hybrid functional, *J. Chem. Phys.* 121 (2004) 1187–1192. <https://doi.org/10.1063/1.1760074>.

[56] M. Mushtaq, M.A. Sattar, S.A. Dar, Phonon phase stability, structural, mechanical, electronic, and thermoelectric properties of two new semiconducting quaternary Heusler alloys COCuZRZ (Z = Ge and Sn), *Int. J. Energy Res.* 44 (2020) 5936–5946. <https://doi.org/10.1002/er.5373>.

[57] M. Born, K. Huang, M. Lax, Dynamical Theory of Crystal Lattices, *Am. J. Phys.* 23 (1955) 474–474. <https://doi.org/10.1119/1.1934059>.

[58] R. Hill, The Elastic Behaviour of a Crystalline Aggregate, *Proc. Phys. Soc. Sect. A* 65 (1952) 349–354. <https://doi.org/10.1088/0370-1298/65/5/307>.

[59] H. Fu, D. Li, F. Peng, T. Gao, X. Cheng, Ab initio calculations of elastic constants and thermodynamic properties of NiAl under high pressures, *Comput. Mater. Sci.* 44 (2008) 774–778. <https://doi.org/10.1016/j.commatsci.2008.05.026>.

[60] O.L. Anderson, A simplified method for calculating the debye temperature from elastic constants, *J. Phys. Chem. Solids* 24 (1963) 909–917. [https://doi.org/10.1016/0022-3697\(63\)90067-2](https://doi.org/10.1016/0022-3697(63)90067-2).

- [61] P. Yan, G. Gao, G. Ding, D. Qin, Bilayer MSe_2 ($M = Zr, Hf$) as promising two-dimensional thermoelectric materials: a first-principles study, *RSC Adv.* 9 (2019) 12394–12403. <https://doi.org/10.1039/C9RA00586B>.
- [62] M. Cutler, N.F. Mott, Observation of Anderson Localization in an Electron Gas, *Phys. Rev.* 181 (1969) 1336–1340. <https://doi.org/10.1103/PhysRev.181.1336>.
- [63] A.N. Gandi, U. Schwingenschlög, WS_2 As an Excellent High-Temperature Thermoelectric Material, *Chem. Mater.* 26 (2014) 6628–6637. <https://doi.org/10.1021/cm503487n>.
- [64] Anisha, R. Kumar, S. Srivastava, K. Tankeshwar, Thermoelectric properties of PtX_2 ($X = Se, Te$) monolayers, *Indian J. Phys.* (2023). <https://doi.org/10.1007/s12648-023-02727-7>.
- [65] D.G. Cahill, S.K. Watson, R.O. Pohl, Lower limit to the thermal conductivity of disordered crystals, *Phys. Rev. B* 46 (1992) 6131–6140. <https://doi.org/10.1103/PhysRevB.46.6131>.
- [66] G. Tan, F. Shi, S. Hao, L.-D. Zhao, H. Chi, X. Zhang, C. Uher, C. Wolverton, V.P. Dravid, M.G. Kanatzidis, Non-equilibrium processing leads to record high thermoelectric figure of merit in $PbTe$ – $SrTe$, *Nat. Commun.* 7 (2016) 12167. <https://doi.org/10.1038/ncomms12167>.
- [67] S.-D. Guo, A.-X. Zhang, Potential 2D thermoelectric materials $ATeI$ ($A=Sb$ and Bi) monolayers from a first-principles study, *Nanotechnology* 28 (2017) 445702. <https://doi.org/10.1088/1361-6528/aa8741>.
- [68] H. He, C. Tyson, and S. Bobev, “Eight-Coordinated Arsenic in the Zintl Phases $RbCd_4As_3$ and $RbZn_4As_3$: Synthesis and Structural Characterization,” *Inorg. Chem.*, vol. 50, no. 17, pp. 8375–8383, Sep. 2011, doi: 10.1021/ic2009418.

- [69] U. Müller, *Inorganic Structural Chemistry*, 1st ed. Wiley, 2006. doi: 10.1002/9780470057278.
- [70] P. Mandal, A. Choudhury, A. B. Mallick, and M. Ghosh, “Phase Prediction in High Entropy Alloys by Various Machine Learning Modules Using Thermodynamic and Configurational Parameters,” *Met. Mater. Int.*, vol. 29, no. 1, pp. 38–52, Jan. 2023, doi: 10.1007/s12540-022-01220-w.
- [71] G. K. H. Madsen, J. Carrete, and M. J. Verstraete, “BoltzTraP2, a program for interpolating band structures and calculating semi-classical transport coefficients,” *Comput. Phys. Commun.*, vol. 231, pp. 140–145, Oct. 2018, doi: 10.1016/j.cpc.2018.05.010.
- [72] V. Schmidt et al., “Using the Seebeck coefficient to determine charge carrier concentration, mobility, and relaxation time in InAs nanowires,” *Appl. Phys. Lett.*, vol. 104, no. 1, p. 012113, Jan. 2014, doi: 10.1063/1.4858936.

PROOF AND SCOPUS INDEXING

6/1/24, 4:58 PM

Publication

 **2nd International Conference
On RAFM-2024**



**2nd International Conference on
RECENT ADVANCES IN FUNCTIONAL MATERIALS
(RAFMs-2024)
14-16 March 2024**

Organized by:
Department of Physics & IQAC, Atma Ram Sanatan Dharma College, (University of Delhi)
Dhaulta Kuan, New Delhi, INDIA-110021

PUBLICATION

Research papers presented in the conference and accepted after review through due process will be published in the Scopus indexed and peer-reviewed journals.



- Springer Nature (SCOPUS)
- IONICS, Springer (SCOPUS)



- Current Natural Science & Engineering, VBF

PLAGIARISM

Similarity Report

PAPER NAME

thesis-1.docx

WORD COUNT

14507 Words

CHARACTER COUNT

80826 Characters

PAGE COUNT

62 Pages

FILE SIZE

13.0MB

SUBMISSION DATE

May 30, 2024 7:10 AM GMT+5:30

REPORT DATE

May 30, 2024 7:12 AM GMT+5:30

● 9% Overall Similarity

The combined total of all matches, including overlapping sources, for each database.

- 5% Internet database
- 5% Publications database
- Crossref database
- Crossref Posted Content database
- 5% Submitted Works database

● Excluded from Similarity Report

- Bibliographic material
- Small Matches (Less than 10 words)
- Manually excluded text blocks

Summary

